10386–10405 *Nucleic Acids Research, 2016, Vol. 44, No. 21* *Published online 29 September 2016*
doi: 10.1093/nar/gkw859

Analyzing structure–function relationships of artificial and cancer-associated PARP1 variants by reconstituting TALEN-generated HeLa *PARP1* knock-out cells

Lisa Rank[1,†], Sebastian Veith[1,2,†], Eva C. Gwosch[3,4], Janine Demgenski[1], Magdalena Ganz[3,4], Marjolijn C. Jongmans[5,6], Christopher Vogel[1], Arthur Fischbach[1,4], Stefanie Buerger[7], Jan M.F. Fischer[1,4], Tabea Zubel[1,4], Anna Stier[1], Christina Renner[1], Michael Schmalz[8], Sascha Beneke[1,9], Marcus Groettrup[7,10], Roland P. Kuiper[5], Alexander Bürkle[1], Elisa Ferrando-May[3] and Aswin Mangerich[1,*]

[1]Molecular Toxicology Group, Department of Biology, University of Konstanz, D-78457 Konstanz, Germany, [2]Research Training Group 1331, Department of Biology, University of Konstanz, D-78457 Konstanz, Germany, [3]Bioimaging Center, Department of Biology, University of Konstanz, D-78457 Konstanz, Germany, [4]Konstanz Research School Chemical Biology, Department of Biology, University of Konstanz, D-78457 Konstanz, Germany, [5]Department of Human Genetics, Radboud University Medical Center Nijmegen, Nijmegen Centre for Molecular Life Sciences, Nijmegen, The Netherlands, [6]Department of Medical Genetics, University Medical Center Utrecht, Utrecht, The Netherland, [7]FlowKon FACS Facility, Department of Biology, University of Konstanz, D-78457 Konstanz, Germany, [8]Center of Applied Photonics, Department of Physics, Department of Biology, University of Konstanz, D-78457 Konstanz, Germany, [9]Ecotoxicology Group, Department of Biology, University of Konstanz, D-78457 Konstanz, Germany and [10]Immunology Group, Department of Biology, University of Konstanz, D-78457 Konstanz, Germany

Received February 02, 2016; Revised September 05, 2016; Accepted September 16, 2016

ABSTRACT

Genotoxic stress activates PARP1, resulting in the post-translational modification of proteins with poly(ADP-ribose) (PAR). We genetically deleted *PARP1* in one of the most widely used human cell systems, i.e. HeLa cells, via TALEN-mediated gene targeting. After comprehensive characterization of these cells during genotoxic stress, we analyzed structure–function relationships of PARP1 by reconstituting *PARP1* KO cells with a series of PARP1 variants. Firstly, we verified that the PARP1\E988K mutant exhibits mono-ADP-ribosylation activity and we demonstrate that the PARP1\L713F mutant is constitutively active in cells. Secondly, both mutants exhibit distinct recruitment kinetics to sites of laser-induced DNA damage, which can potentially be attributed to non-covalent PARP1–PAR interaction via several PAR binding motifs. Thirdly, both mutants had distinct functional consequences in cellular patho-physiology, i.e. PARP1\L713F expression triggered apoptosis, whereas PARP1\E988K reconstitution caused a DNA-damage-induced G2 arrest. Importantly, both effects could be rescued by PARP inhibitor treatment, indicating distinct cellular consequences of constitutive PARylation and mono(ADP-ribosyl)ation. Finally, we demonstrate that the cancer-associated PARP1 SNP variant (V762A) as well as a newly identified inherited PARP1 mutation (F304L\V762A) present in a patient with pediatric colorectal carcinoma exhibit altered biochemical and cellular properties, thereby potentially supporting human carcinogenesis. Together, we establish a novel cellular model for PARylation research, by revealing strong structure–function relationships of natural and artificial PARP1 variants.

*To whom correspondence should be addressed. Tel: +49 7531 884067; Fax: +49 7531 4033; Email: aswin.mangerich@uni-konstanz.de
†These authors contributed equally to this paper as first authors.

INTRODUCTION

Poly(ADP-ribosyl)ation (PARylation) is a post-translational modification that plays key roles in cellular physiology and stress response (1). It mainly occurs in the nucleus and to a lesser extent in the cytoplasm. The reaction is carried out by enzymes of the family of poly(ADP-ribose) polymerases (PARPs), which use NAD^+ to synthesize poly(ADP-ribose) (PAR), a biopolymer with variable chain length and branching. Of the 17 members of the human *PARP* gene family, at least four have been shown to be true PARPs, i.e. these do exhibit PAR-forming capacity, while other family members act as mono-ADP-ribosyl transferases or are catalytically inactive. PARP1 is a highly abundant, chromatin-associated protein that exhibits PARylation activity. Upon binding to DNA damage, in particular to strand breaks, and subsequent conformational rearrangements, PARP1 is catalytically activated and contributes to the bulk of the cellular PAR formation (1). This can happen either in *cis* by activation of a single PARP1 molecule (2,3), or in *trans*, by PARP1 dimerization at sites of DNA damage (4,5). Apart from DNA damage-dependent activation, PARP1 activity is also regulated by post-translational modifications, such as phosphorylation, acetylation, and SUMOylation (6–10), as well as by direct protein-protein interactions (11–14). Catalytic activation leads to covalent PARylation of hundreds of target proteins (15,16), however, PARP1 itself is the main target of its modification (i.e. PARP1 automodification) (17,18). In addition to covalent PARylation, PAR can interact with proteins non-covalently via distinct PAR binding modules (19). Importantly, PARylation is highly dynamic (20,21), because shortly after being synthesized, PAR is rapidly hydrolyzed by poly(ADP-ribose) glycohydrolase (PARG) and other catabolizing enzymes (22). Thereby, PARylation transiently modulates physico-chemical properties and spatio-temporal activities of target proteins, including chromatin and DNA repair factors, as well as PARPs themselves (23,24). On the cellular level, PARylation fulfills pleiotropic functions in genome maintenance, including DNA repair, telomere length regulation and re-initiation of stalled replication forks (25). Moreover, it is involved in a host of further cell functions, such as chromatin remodeling, transcription, epigenetics, signaling, cell cycle, and regulation of cell death. There is also evidence that some functions of PARP1 are independent of its enzymatic activity, such as its action as a co-activator or repressor of certain transcription factors (1). On the organismic level, these functions link PARP1 and PARylation to mechanisms of inflammation and metabolism, as well as aging and cancer biology (24,25). Notably, several PARP inhibitors are currently being tested in clinical cancer therapy, either in combination with classical chemo- or radiotherapy or as stand-alone drugs following the concept of synthetic lethality in *BRCA1/2* deficient tumors. Recently, the PARP inhibitor olaparib has been approved by the EMA and FDA for the use in certain *BRCA*-mutated ovarian cancers (26,27).

A lot of our knowledge on PARP1 and PARylation has been obtained through a series of studies using three independently generated *Parp1* knock-out mouse models and immortalized mouse embryonic fibroblasts (MEFs) derived thereof (28–31), as well as siRNA-based knock-down approaches (32). Strikingly, a genetic double knock-out of *Parp1* and *Parp2* resulted in embryonic lethality in the mouse, thereby demonstrating a key function of PARylation during development (33). To the best of our knowledge, besides a very recent report on a CRISPR/Cas-generated *PARP1* knock-out in HEK cells (34), genetic deletion of *PARP1* in human cancer cell lines has so far not been described. Notably, at present no *PARP1* mutations have been directly related to human hereditable diseases – presumably because such mutations lead to embryonic lethality beforehand. Yet, several *PARP1* polymorphisms exist that have been associated with an increased risk for cancer development and inflammatory diseases. For example, a *PARP1* polymorphism, causing the amino acid exchange (aa) V762A (35), leads to reduced enzymatic activity of purified recombinant PARP1 protein (36,37). Notably, the PARP1\V762A variant is associated with an increased risk for the development of several types of cancers in specific ethnicities (38,39). How the V762A variant and other potentially disease-associated *PARP1* polymorphisms and mutations affect cellular PARP1 activities and functions is so far unknown.

Here, we report a genetic knock-out of *PARP1* in one of the most widely used human cell systems, i.e. HeLa cells, via TALEN-mediated gene targeting. We characterized these cells with regards to PARylation metabolism and genotoxic stress resistance. By reconstituting HeLa *PARP1* KO cells with a series of PARP1 variants, we then analyzed structure–function relationships of PARP1 variants in a cellular environment without interfering with endogenously expressed WT-PARP1. These variants included sets of artificial mutants and natural variants to illustrate the potential of this system for its wider usage in PARylation research. The first set included two artificial PARP1 mutants that are of high interest to understand the cellular biochemistry of PARylation, i.e. a hypomorphic (E988K) and a hypermorphic (L713F) PARP1 mutant. Using a second set of PARP1 variants, we then analyzed cellular consequences of naturally occurring PARP1 variants, i.e. the PARP1 polymorphism leading to the V762A aa exchange and a newly identified germline PARP1 mutant (F304L) in a patient with pediatric colorectal carcinoma (*NB.* in addition the patient carried the V762A polymorphism and a pathogenic mutation in *BRCA2*). Further, we characterized functional consequences of the PARP1-reconstitution in HeLa *PARP1* KO cells to improve our understanding on the significance of PARP1 and PARylation in (patho-)physiology.

MATERIALS AND METHODS

Generation of HeLa *PARP1* KO cells by TALEN-mediated gene targeting

Cells were cultured in DMEM supplemented with 10% FBS, 2 mM L-glutamine and 1% penicillin/streptomycin at 37°C, 5% CO_2 and 95% humidity. TALENs were custom synthesized by Cellectis Bioresearch and were designed to target the first exon of the *PARP1* gene in close proximity to the start codon (Supplementary Figure S1). For

the generation of stable *PARP1* KO cell lines, HeLa Kyoto cells were transfected with 1 μg of each TALEN arm DNA using Effectene transfection reagent (Qiagen). After 24 h, cells were subcloned using a limited dilution approach. Briefly, TALEN-transfected cells were trypsinized and diluted to a concentration of 1000 cells/ml. From this dilution, three different sub-dilutions were prepared (100 cells/ml, 30 cells/ml, and 5 cells/ml) and each one seeded into a 96-well plate (100 μl per plate). After 5–8 days, the plates were examined for the formation of cell colonies. Only wells with one single colony were selected for further processing. Clones were screened for a reduction in PARP1 expression via immunofluorescence analysis (see below). Two rounds of TALEN-transfection and clonal expansion were necessary to target all PARP1 alleles present in the HeLa genome. Complete ablation of PARP1 expression in individual clones was verified by Western blotting. The parental HeLa Kyoto cell line was used as a wild-type (WT) control.

Orthologous expression and purification of recombinant *PARP1*

Baculovirus expression constructs of PARP1 were generated according to manufacturer's instructions (BD). Recombinant (rec.) PARP1 was overexpressed in *Sf*9 insect cells with an MOI of 1 for 60 h. Thereafter, cells were harvested, pelleted and stored at −80°C. Rec. PARP1 was purified as described previously (40), with modifications. Briefly, cell pellets were lysed for 20 min in lysis buffer (1 ml per 1.5×10^7 cells; 25 mM Tris–HCl pH 8.0, 10 mM EDTA pH 8.0, 50 mM glucose, 0.2% Tween 20, 0.2% NP-40, 0.5 M NaCl, 1 mM PMSF and 1 mM 2-mercaptoethanol) and cell debris was cleared by centrifugation at 20 000 × *g* for 20 min. Protamine sulfate (1 mg/ml) was added to the supernatant and samples centrifuged again for 10 min at 20 000 × *g*. Next, ammonium sulfate was added to 30% saturation, followed by centrifugation at 25 000 × *g* for 20 min. Ammonium sulfate saturation in the supernatant was increased to 80%, and centrifuged again at 20 000 × *g* for 15 min. For desalting, the PARP1 containing pellet was dissolved in Buffer 2 (1 ml per 1.5×10^7 cells; 100 mM Tris–HCl pH 7.4, 0.5 mM EDTA pH 7.4, 10% glycerol, 1 mM PMSF and 2 mM 2-mercaptoethanol) and loaded onto a Sephadex G-100 column (Sigma-Aldrich). Proteins were eluted with 10 ml Buffer 3 (50 mM Tris–HCl pH 8.0, 0.5 mM EDTA pH 8.0, 5 mM $MgCl_2$, 5% glycerol, 1 mM PMSF and 2 mM 2-mercaptoethanol) and fractions were separated on a 10% SDS gel, followed by Coomassie staining and western blotting to identify the PARP1 containing fractions. These fractions were pooled and loaded onto a dsDNA-cellulose column (Sigma-Aldrich). Proteins were eluted with Buffer 3, containing increasing concentrations of KCl (100 mM, 200 mM, 400 mM and 1 M). The PARP1 fractions were pooled and concentrated using an Amicon 50-kD cut-off spin filter, for buffer exchange (storage buffer, 20% glycerol in PBS). Protein concentration was determined using the Bradford assay and the purified rec. PARP1 samples were aliquoted, snap-frozen in liquid nitrogen and stored at −80°C until further usage.

PARP1 activity assay

PARP1 activity was performed as previously described (37), with modifications. Reaction buffer (100 mM Tris–HCl pH 7.8, 1 mM DTT, 10 mM $MgCl_2$ and 25 μg/ml of double-stranded DNA activator oligonucleotide, i.e. EcoRI linker) was pre-incubated at 30°C for 60 s. The reaction was started by addition of 5 nM PARP1 and varying concentrations of NAD^+ (50–400 μM) and was stopped by addition of an equal volume ice-cold 20% TCA. Each sample (15% of total) was loaded per slot in a slot-blot manifold in technical triplicates and vacuum aspirated on a Hybond-N^+ nylon membrane (GE Healthcare). Purified PAR in different concentrations (200–1500 fmol) was applied as technical standards. The slots were washed with 10% TCA and 70% ethanol before heat-crosslinking for 1 h at 90°C. Afterwards, the membrane was blocked in M-TNT, followed by incubation with anti-PAR antibody 10H (1:300 in M-TNT) for 1 h. Next, the membrane was washed thrice in TNT for 5 min, followed by incubation with secondary antibody goat anti-mouse-HRP (1:2000 in M-TNT) for 1 h. The membrane was again washed thrice in TNT, followed by chemiluminescence detection at LAS 4000 mini (GE Healthcare). The band intensities were evaluated densitometrically using ImageJ software.

In silico search for PAR binding motifs

PARP1 was screened for PAR-binding motifs (PBMs) using the PATTINPROT tool (https://npsa-prabi.ibcp.fr/cgi-bin/npsa_automat.pl?page=npsa_pattinprot.html) as described previously (41). The PBM-pattern [HKR]-X-[AVILFWP]-[AVILFWP]-[HKR]- [HKR]-[AVILFWP]-[AVILFWP] (42) was searched against the full-length protein sequence of PARP1 (http://www.uniprot.org/; P09874 PARP1_HUMAN), allowing for one (PBM1) or two mismatches (PBM2).

Far-western PAR binding assay

Rec. PARP1 was either size-separated using SDS-PAGE and subsequent Western blotting on a PVDF membrane, vacuum-aspirated onto a nitrocellulose membrane using a slot-blot manifold (Roth), or, in case of the peptide studies, purchased as a membrane with covalently attached peptides (PepSpot membrane with on-membrane synthesized peptides, JPT Technologies). The PepSpot membrane was activated in 100% methanol for 5 min according to the manufacturer's instructions, followed by a 5-min wash in TNT [150 mM NaCl, 10 mM Tris–HCl pH 8.0, 0.05% (v/v) Tween 20] and a 1-h incubation in TNT. The membrane was then incubated over night with 0.2 μM unfractionated PAR in TNT at 4°C. Negative controls were incubated with TNT only, i.e. w/o PAR. The blots were subjected to three 10-min washes with high salt buffer to remove non-specifically bound PAR. Next, membranes were washed twice with TNT for 10 min and blocked with 5% milk powder solution in TNT (M-TNT) for 1 h. Subsequently, blots were incubated for 1 h with anti-PAR-specific primary antibody 10H (1:300 in M-TNT), followed by three 5-min TNT washes. The blots were then incubated for 1 h with secondary antibody goat anti-mouse-HRP (Dako Cytomation, 1:2000 in

M-TNT), followed by three 5-min washes in TNT and subsequent chemiluminescence detection. Slot-blot and western blots were stripped, blocked again, and re-probed with mouse anti-PARP1 antibody CII-10 (1:300 in M-TNT) as loading control.

Biotinylation and size-fractionation of PAR

Biotinylation of PAR was performed as described previously (43) with some modifications. Briefly, 400 μM of purified PAR were incubated for 8 h at RT in a buffer consisting of 100 mM sodium acetate buffer pH 5.5, 1 mM $NaBH_3CN$, 4 mM EZ-Link Hydrazide-Biocytin (Thermo Scientific). After dialysis against 100 mM sodium acetate buffer pH 5.5 with a 2 kDa cut-off Slide-A-Lyzer Dialyis cassette G2 (Thermo Scientific), PAR was ethanol-precipitated. Concentration of PAR was determined via UV absorbance measurements at 258 nm. The biotinylated PAR was separated from non-biotinylated PAR by affinity purification using the Pierce Monomeric Avidin Kit (Thermo Scientific) according to the manufacturer´s instructions. The elution fractions were dialyzed against 100 mM sodium acetate buffer pH 5.5 followed by ethanol-precipitation. HPLC fractionation of the biotinylated PAR was performed as described previously (43). Briefly, the biotinylated PAR was fractionated using an Agilent 1100 series HPLC with a semi-preparative DNAPac™ PA100 BioLC column (Thermo Scientific), by applying a multistep NaCl gradient in 25 mM Tris–HCl pH 9.0, modified from (43). The 258 nm UV absorbance signal was used to collect PAR fractions manually, followed by ethanol-precipitation.

Electrophoretic mobility shift assays (EMSAs)

DNA-EMSAs were performed as described previously (41). Briefly, rec. PARP1 was incubated for 20 min with 200 fmol biotinylated double-stranded DNA oligonucleotide [5′-biotin-$(TTT)_5$-TTAGGGTTAGGGTTAGGGTTAG GGCATGCACTAC-3′ and 5′-GTAGTGCATGCCCT AACCCTAACCCTAACCCTAA-$(TTT)_5$-3′] in EMSA buffer (40 mM Tris–HCl pH 8.0, 5 mM DTT, 4 mM $MgCl_2$, 0.1 mg/ml BSA and 0.1% NP-40) at RT. Then, samples were mixed with 10× loading dye (40% glycerol, 0.05% orangeG and 0.05% bromphenol blue) and loaded on a 5% native TBE gel. The gel was blotted onto a nylon membrane, followed by heat-crosslinking (1 h at 90°C). The blot was blocked for 1 h in M-TNT, washed thrice for 5 min in TNT and then incubated for 1 h with streptavidin-HRP (1:1000 in TNT). Afterwards, membranes were washed thrice for 5 min in TNT followed by chemiluminescence detection. When the effect of PAR binding on PARP's DNA binding ability was tested, PARP1 was pre-incubated with unfractionated PAR (in amounts as indicated) for 20 min at RT before addition of the DNA substrate. The band intensities were analyzed using ImageJ to calculate relative band shifts.

PAR-EMSAs were essentially performed as described previously (43), with modifications. Briefly, rec. PARP1 in increasing concentration was mixed with EMSA buffer (see above) and incubated at 25°C for 10 min. After addition of 500 fmol size-fractionated biotinylated PAR (30–35 mer) the samples were again incubated at 25°C for 20 min. The samples were mixed with 10× loading dye (40% glycerol and 0.05% orangeG), separated on a 5% native TBE gel by electrophoresis, semi-dry blotted on nylon membrane, followed by drying at 90°C for 1 h. After 1-h blocking in M-TNT, the blots were washed thrice for 5 min with TNT followed by an 1-h incubation with streptavidin-HRP (1:1000 in TNT). Afterwards, the blots were washed again thrice with TNT, followed by chemiluminescence detection.

Identification of F304L variant in a patient with pediatric colorectal carcinoma

This patient, with non-polyposis, microsatellite stable colorectal cancer, diagnosed at 13 years of age, was included in a study to identify novel CRC predisposing genes by applying exome sequencing on germline DNA. Clinical data, tumor tissue and DNA samples were obtained. The patient and the parents provided informed consent and the studies were approved by the Medical Ethics Committee of the Radboud University Medical Center in Nijmegen (no. 2012/271). DNA was extracted from peripheral blood cells and tumor tissues using standard procedures.

The exome sequencing procedures used were essentially as reported before (44). Briefly, exome enrichment was performed using an AB SOLiD optimized SureSelect human exome kit v1 (Agilent). Small insertions and deletions were detected using the SOLiD Small InDel Tool. All variants were annotated using an in-house developed analysis pipeline (44,45). For prioritization, we selected high confident non-synonymous variants that had a high probability of being pathogenic, and were absent in dbSNPv132 and our in-house variant database containing at time of analysis 1302 in-house analyzed exomes. The candidate mutations were validated by Sanger sequencing in peripheral blood DNA of the child and its parents.

Generation of *PARP1*-GFP expression constructs and cell transfection

PARP1 mutants were generated by site-directed mutagenesis (mutated bases are marked by bold underlining). Plasmids pET15b::PARP1\V762 and pET15b::PARP1\A762 were used as templates to generate the mutants pET15b::PARP1\V762\L304 and pET15b::PARP1\A762\L304 using the primer pair 5′-AATGCTCGGGTCAGCTGGTC**C**TCAAGAGC-3′ and 5′-GCAGTAATAGGCA**T**CGCTCTTGA**G**GA CCAGCT-3′. For rec. protein expression in *Sf*9 cells the *PARP1* sequences were PCR-extracted (5′- AAAC TGGCGGCCGCATGGCGGAGTCTTCGGATAAGC-3′ and 5′-TCGAGTGCGGCCGCTTACCACAGG GAGGTCTTAA-3′) and sub-cloned into the pJET1.2 vector using the CloneJET PCR cloning kit (Thermo Fisher), thereby introducing NotI restriction sites up- and downstream of the *PARP1* sequences (underlined in primer sequence). Using these restriction sites the *PARP1* sequences were cloned into the MCS of the baculovirus expression vector pVL1393 (BD). peGFP-N1::PARP1\V762A, peGFP-N1::PARP1\F304L and peGFP-N1::PARP1\F304L\V762A were generated using the pVL1393 plasmids as donors. Therefore, the

respective pVL1393 plasmids and pEGP-N1::PARP1 were digested with BssHII and EcoRV. The resulting fragments were ligated in the pEGP-N1::PARP1 backbone. peGFP-N1::PARP1\E988K and peGFP-N1::PARP1\L713F were generated by site-directed mutagenesis using peGFP-N1::PARP1 as a template. For peGFP-N1::PARP1\E988K the primer pair 5′-CCTCTCTACTATATAAC**A**AGTACATTGTCT-3′ with 5′-CATAGACAATGTACT**T**GTTATATAGTAGAG-3′ was used. For peGFP-N1::PARP1\L713F the primer pair 5′-GCATACTCCATC**T**TCAGTGAG-3′ with 5′-GGACCTCACTGA**A**GATGGAG-3′ was used. Correct orientation of the inserts and successful mutagenesis were verified by DNA sequencing (GATC Biotech).

For reconstitution experiments, *PARP1* KO cells were transfected with different eGFP-N1::PARP1 plasmids using Effectene (Qiagen), according to the manufacturer's instructions. Briefly, DNA, EC-buffer and Enhancer were carefully mixed and incubated for 4 min. Next Effectene was added and the solution was again carefully mixed. After incubation for 10 min at room temperature cell culture medium was added and the transfection mix was pipetted dropwise onto the cells. In order to mitigate cytotoxicity of the transfection the medium was exchanged 12–16 h after transfection.

Immuno-chemical detection of *PARP1* and PAR by fluorescence microscopy

HeLa WT and HeLa *PARP1* KO cells were seeded on glass cover slips in 12-well plates. PAR formation was induced by H_2O_2 treatment for 5 min, 48 h after transfection. After treatment, cells were washed once with PBS and fixed in 4% (w/v) PFA in PBS for 20 min. All subsequent incubation steps were performed at RT on a shaker. In order to stop fixation, 100 mM glycine in PBS was added for 1 min followed by washing of the slides in PBS. For permeabilization, the slides were incubated for 3 min in 0.4% Triton X-100 in PBS, followed by washing with PBS.

For immunofluorescence staining, the cells were blocked in PBS containing 20% (w/v) non-fat milk powder and 0.2% (v/v) Tween 20 (PBSMT) for 1 h. Then, samples were either incubated with the primary antibodies mouse-anti-PAR (10H) or mouse-anti-PARP1 (FI-23 or CII-10) at 37°C for 1 h. Subsequently, the slides were washed thrice for 10 min in PBS, followed by incubation with the secondary antibodies goat anti-mouse IgG coupled to Alexa546 (1:400 in PBSMT). Next, the slides were washed thrice for 10 min in PBS, nuclei were stained with Hoechst33342 (0.1 μg/ml in PBS) for 5 min, slides were washed again in PBS thrice for 10 min, and mounted with Aqua Poly/Mount (Polysciences Inc.). Microscopic images were acquired using a Zeiss Axiovert 200M microscope. Image data for PARP1 and PAR was analyzed using an automated KNIME workflow. Antibody controls, prepared without the primary antibody were used to determine background fluorescence. Only cells with a GFP fluorescence intensity higher than 1.5-fold of the mean background fluorescence intensity were considered GFP-positive and analyzed for PAR-fluorescence.

Western blot analysis

Protein lysates of PARP1-transfected HeLa *PARP1* KO cells were prepared about 40 h after transfection. To this end, cells were trypsinized, counted and 5×10^5 cells were centrifuged. The pellet was resuspended in 33 μl PBS containing 1× complete protease inhibitor cocktail (Roche) and lysed by addition of 66 μl SDS loading dye (93.75 mM Tris-HCl (pH 6.8), 9 M urea, 7.5% (v/v) β-mercaptoethanol, 15% (v/v) glycerol, 3% (w/v) SDS and 0.01% (w/v) bromphenol blue). DNA was sheared through syringes with decreasing diameters and 30 μl protein lysates were loaded per lane, run on 10% SDS gels, and semi-dry blotted onto a nitrocellulose membrane. Membranes were blocked for 1 h in M-TNT or in TNT with 5% BSA (in case of antibodies detecting phosphorylated proteins), followed by 1-h incubation with primary antibodies [mouse anti-PARP1 CII-10 (1:300); mouse-anti-p53 (1:1000, Merck Millipore); rabbit-anti-p16 (1:2000, Abcam mouse anti-actin (1:50 000, Millipore) in M-TNT and rabbit anti-ph-p53(Ser15) (1:1000, Cell Signaling); mouse-anti-γH2A.X (1:2000, Millipore) both in TNT with 5% BSA, rabbit anti-phospho-RPA2 (Ser4/8) (Sigma-Aldrich)] and three 5-min washes in TNT. Next, membranes were incubated 1 h with the respective secondary antibodies [goat-anti rabbit-HRP 1:2000 in M-TNT (Dako); goat-anti mouse-HRP 1:2000 or 1:5000 in M-TNT (Dako)], again followed by three 5-min washes in TNT and chemiluminescence detection.

LC–MS/MS quantitation of cellular PAR

Quantitation of cellular PAR levels by isotope dilution mass spectrometry (LC–MS/MS) was conducted as described previously (20), with modifications. Briefly, cells were treated with H_2O_2 in concentrations as indicated for 5 min at 37°C. Then, cells were washed briefly with ice-cold PBS, placed on ice and lysed with 1 ml 20% TCA. The lysed cells were harvested using a cell scraper and centrifuged for 5 min at 3000 × *g* and 4°C. The supernatant was discarded, the pellet washed twice with 500 μl ice-cold 70% ethanol and centrifuged for 5 min at 3000 × *g* at 4°C. The pellet was air-dried at 37°C, resuspended in 255 μl 0.5 M KOH by constant shaking until completely dissolved and was then neutralized with 50 μl 4.8 M MOPS buffer. For determination of DNA concentration, 30 μl were removed. To each 30-μl sample, 390 μl MOPS:KOH (1 M:0.5 M) and 2.1 μl Hoechst 33342 (1 mg/ml) were added and fluorescence intensities were measured with an extinction wavelength of 360 nm and an emission wavelength of 460 nm utilizing a VarioskanFlash Fluorescence Reader (Thermo Scientific). The DNA concentration of a sample was calculated using a standard curve from defined amounts of calf thymus DNA (Sigma-Aldrich). Heavy-isotope labeled, undigested PAR (12 pmol) was added as an internal standard. DNA and RNA were digested for 3 h at 37°C by incubating samples with 0.1 mg/ml DNase 1 (Roche), 0.1 mg/ml RNase A (Sigma-Aldrich), 50 mM $MgCl_2$ and 100 mM $CaCl_2$. Then, 1.25 μl of 40 mg/ml proteinase K (Roche) were added and samples were incubated at 37°C over night. Thereafter, PAR was purified using the High Pure miRNA Isolation kit (Roche) according to the manufacturer's instructions. PAR was eluted in 100 μl RNase-free water and then digested

into its subunits with 10 U PDE1 (Affymetrix) and 0.5 U alkaline phosphatase (Sigma-Aldrich) for 3 h at 37°C. Next, the samples were filtered through a 10-kD Nanosep filter (Pall) and subsequently dried in a speedvac. The samples were then resolved in 100 μl MilliQ water and subjected to LC–MS/MS analysis.

NAD^+ cycling assay

HeLa WT or HeLa *PARP1* KO1 cells were seeded in 6-well plates and transfected with the different eGFP-N1::PARP1 plasmids using Effectene (Qiagen). Two days after transfection, NAD^+-cycling assays were performed. To this end, PAR formation was induced by treatment with 500 μM H_2O_2 for 8 min. Cells were harvested using trypsin/EDTA and kept on ice during all subsequent steps. The cell numbers were determined using a CASY cell counter (Roche) and 5×10^5 cells were used for analysis. Cell pellets were resuspended in 500 μl PBS and lysed by addition of 24 μl 3.5 M perchloric acid. After a 15-min incubation, samples were centrifuged to remove cellular debris. The supernatant was mixed with 350 μl phosphate buffer (0.33 mM K_2HPO_4, 0.33 mM KH_2PO_4 pH 7.5) followed by a 15-min incubation to allow precipitation. After centrifugation, the supernatant was incubated on ice for 20 min followed by another round of centrifugation. The resulting supernatant was used in the NAD^+-cycling assay. As a reference, a standard curve was determined in each experiment. To this end, NAD^+ was diluted to concentrations ranging for 0 μM to 0.48 μM. Each sample was measured in technical triplicates and therefore 40 μl of the supernatant were diluted in 160 μl Diluent (0.5 M H_3PO_4, 0.5 M NaOH). To each well 100 μl of a reaction mix [0.48 M bicine (pH8), 4 mg/ml BSA, 0.02 M EDTA, 2.4 M ethanol, 2 mM MTT, 0.96 mg alcohol dehydrogenase and 5.7 mM phenazine ethosulfate] was added. Absorption at 550 nm was measured after a 30-min incubation at 30°C using 690 nm as a reference wavelength. The intracellular NAD^+ concentration was calculated with the help of the standard curve and normalized to the transfection efficiencies as determined by FACS analysis performed in parallel according to the following formula:

$$n\,(\mathrm{NAD^+}\ in\ \mathrm{KO1}) \times (1 - \text{transfection efficiency}) + n\,(\mathrm{NAD^+}\ \text{in transfected cells}) \times \text{transfection efficiency} = n\,(\mathrm{NAD^+}\ \text{measured})$$

Cell proliferation and viability analysis

For the Alamar Blue assay, a number of 4000 cells were seeded into a 96-well plate in technical triplicates and incubated for 4 h at 37°C (defined as time point '0 h'). At subsequent time points, Alamar Blue solution (Invitrogen) was added and cells were incubated for an additional hour at 37°C. The fluorescence signal was measured at 550 nm excitation wavelength and 590 nm emission wavelength and data normalized to the '0 h' time point.

For annexin V /PI staining, HeLa WT and *PARP1* KO cells were seeded in 6-well plates and transfected with the different eGFP-N1::PARP1 plasmids using Effectene (Qiagen). In case of treatment, camptothecin (CPT; Sigma-Aldrich) or DMSO as solvent control were added to the medium 24 h after transfection. Two days after treatment, cells were harvested using trypsin/EDTA. The used medium, the PBS, and the trypsin/EDTA with the fresh medium were collected. The resulting cell concentration was determined using a CASY cell counter (Roche). A number of 2.5×10^5 cells was pelleted and resuspended in annexin V binding buffer (10 mM HEPES pH 7.4, 140 mM NaCl, 2.5 mM $CaCl_2$). A volume of 195 μl of the cell suspension was mixed with 5 μl annexin V-FITC (for untransfected cells) or annexin V-APC (for transfected cells) and incubated in the dark at RT. Finally, 200 μl of propidium iodide (PI) solution (10 μg/ml PI in annexin V binding buffer) were added and the cells were analyzed using a FACSCalibur (BD). For each sample, 10 000 transfected cells were analyzed. Only GFP-positive cells were included in the analyses.

Cell cycle analysis

HeLa WT or HeLa *PARP1* KO cells were seeded in 6-well plates and transfected with the different eGFP-N1::PARP1 plasmids using Effectene (Qiagen). Three days after transfection, the cells were harvested using trypsin/EDTA, pelleted, and resuspended in 300 μl PBS. Then, 700 μl ethanol were added for fixation, cells were incubated for 20 min followed by centrifugation. The pellet was washed with PBS, centrifuged again and resuspended in 30 μl PBS. A volume of 120 μl of DNA extraction buffer (4 mM citric acid, 0.2 M Na_2HPO_4, pH 7.8) was added and the samples were incubated for 20 min on a shaker at RT. After centrifugation the samples were resuspended in PI-staining solution (PBS, 0.2 mg/ml RNAase A, 20 μg/ml PI) and analyzed using a FACSCalibur (BD). For each sample, 10 000 transfected cells were measured. Only GFP-positive cells were included in the analyses.

Clonogenic survival assay

Cells (1×10^6 cells/ml) were incubated for 5 min in the presence of H_2O_2 in concentrations as indicated. Subsequently, 500 cells were seeded in 6-cm plates and incubated at 37°C, 5% CO_2 and 95% humidity. After 2 weeks, medium was removed and colonies were fixed and stained for 1 h using a 10%-formaldehyde solution (Sigma-Aldrich) mixed with 0.1% crystal violet. The culture dishes were washed and colonies consisting of at least 20 cells were counted using a stereomicroscope (Leica).

Live imaging of *PARP1* recruitment to sites of laser-induced DNA damage

For the analysis of recruitment to DNA damage, 1×10^5 HeLa *PARP1* KO cells were seeded on μ-slides (ibidi) 24 h before transfection with the different eGFP-N1::PARP1 constructs using Effectene (Qiagen) according to the manufacturer's instructions. Protein expression was allowed for 40 h. On the day of irradiation, the medium was changed to phenol red-free DMEM (Invitrogen).

DNA damage was induced with a commercially available 780 nm femtosecond-pulsed fiber laser (Toptica, Munich, Germany) coupled into a LSM700 confocal laser scanning microscope (Zeiss) through an independent scanner system (Rapp Optoelectronics, Hamburg, Germany). Within the GFP-positive cell nuclei a 6 μm line was irradiated for a total irradiation time of 3.78 sec using 5 mW average power and a repetition rate of 40 MHz. Imaging was performed

using a Zeiss EC-Plan-Neofluar 40×/1.3 oil immersion objective lens at a wavelength of 488 nm through an open pinhole. Acquisition of time lapses at multiple positions was facilitated by an automated macro (LIC macro, University of Freiburg, Germany) and analysis was performed with a line analysis macro for ImageJ which is available for download on http://www.bioimaging-center.uni-konstanz.de (BIC tool box, University of Konstanz, Germany).

Statistical analysis

Statistical testing was performed using GraphPad Prism and tests were applied as indicated in Figure legends. $*P \leq 0.05$, $**P \leq 0.01$, $***P \leq 0.001$.

RESULTS

Generation and characterization of HeLa *PARP1* knock-out cells

We set out to generate a genetic *PARP1* KO in one of the most widely used human cellular model systems, i.e. HeLa cells. Recently the HeLa genome has been fully sequenced (46,47), enabling us to use the TALEN technology to target exon 1 of *PARP1* [MIM 173870] (Supplementary Figure S1). We identified two independent clones, termed *PARP1* KO1 and KO2, that displayed complete abrogation of PARP1 expression, as evaluated by single-cell fluorescence microscopy (Figure 1A) and Western blotting (Figure 1B). DNA sequencing of PCR amplicons of the genomic region of interest confirmed successful targeting by introducing small deletions in *PARP1* exon 1 in both clones (data not shown). To characterize how the loss of PARP1 affects PAR metabolism, we treated HeLa WT and *PARP1* KO clones with doses of 10 μM to 1 mM H_2O_2. As it is evident from single-cell immuno-epifluorescence microscopy using the anti-PAR specific antibody 10H, no PAR signal could be observed in *PARP1* KO cells even at the highest treatment dose of 1 mM H_2O_2 (Figure 1C). Next, we tested if the loss of PARP1 affects NAD^+ levels under non-stress conditions as well as upon H_2O_2 treatment by using an enzymatic NAD^+ cycling assay based on (48). Figure 1D shows that under non-stress conditions the loss of PARP1 did not lead to significant changes in basal NAD^+ levels. As expected, treatment of HeLa WT cells with H_2O_2 led to a dramatic drop in cellular NAD^+ levels. In contrast, NAD^+ levels did not significantly change in *PARP1* KO cells upon H_2O_2 treatment (Figure 1D). To analyze cellular PAR metabolism in greater detail, we used a bioanalytical method based on isotope dilution mass spectrometry, which, in contrast to immunochemical-based technologies, is sensitive enough to quantify basal PAR levels in unstressed cells with unequivocal chemical specificity (20). A 100-fold increase in cellular PAR levels was observed, when HeLa WT cells were treated with up to 200 μM H_2O_2. As expected this effect could be largely inhibited by treating cells with the pharmacological PARP inhibitor ABT888 (10 μM) (Figure 1E). Residual PARP activity in the presence of 10 μM ABT888 has been observed before (20) and can be attributed to the much higher sensitivity of the LC–MS/MS method as compared to the immunofluorescence analysis, which is not able to detect this residual PARP activity (20). HeLa *PARP1* KO cells showed only a 5–7-fold increase in PAR levels, which could be completely inhibited by ABT888 treatment. These results demonstrate that upon induction of severe genotoxic stress, PARP1 contributes to >90% of cellular PAR formation in HeLa cells. The residual PAR forming ability can be probably attributed to other DNA damage dependent PARPs, such as PARP2 and PARP3 (49). Importantly, while stress-induced PAR formation was almost completely abolished in *PARP1* KO cells, basal PAR levels remained constant, indicating that under physiological, non-stress conditions other PARPs can compensate for the loss in PARP1 (insert in Figure 1E). Recently, it has been shown that PARP1 plays a

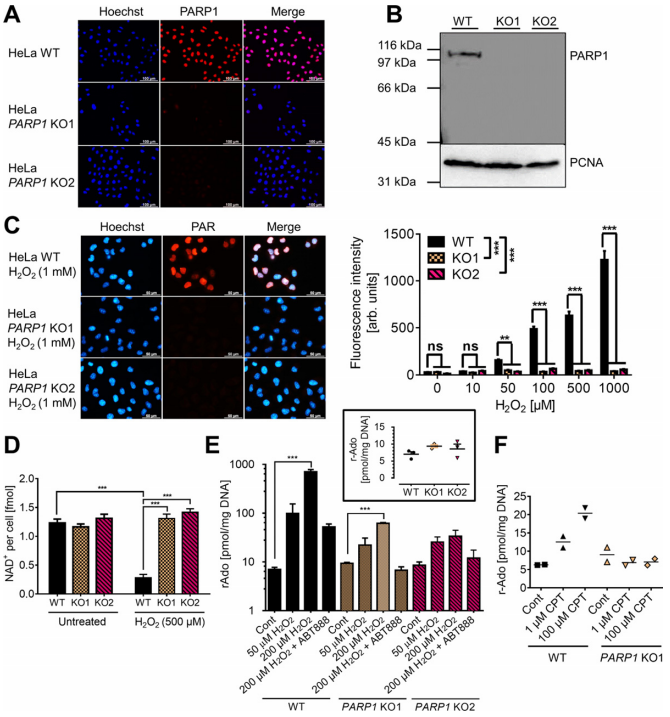

Figure 1. TALEN-mediated gene targeting of *PARP1* in HeLa cells. (**A**) Single-cell immuno-epifluorescence analysis of PARP1 expression in HeLa WT and in two independently generated *PARP1* knock-out (KO) clones (KO1 and KO2). (**B**) Western blot analysis of PARP1 expression in HeLa WT and *PARP1* KO clones. PCNA served as a loading control. (**C**) Single cell immuno-epifluorescence analysis of PAR formation in HeLa WT and *PARP1* KO clones. WT cells showed a dose-dependent increase in cellular PAR levels upon H_2O_2 treatment (for 5 min), while PAR levels in *PARP1* KO cells remained close to background signal intensities. Representative epifluorescent microscopic images (left panel), quantitation of image data (right panel). Means ± SEM, at least 70 cells per data point were analyzed. Statistical analysis was performed via two-way ANOVA testing and Sidak's post-test. (**D**) Intracellular NAD^+ levels in WT and *PARP1* KO cells ± H_2O_2 treatment for 7 min as measured by an enzymatic NAD^+ cycling assay. Means ± SEM of $n = 3$ independent experiments. Statistical analysis was performed using two-way ANOVA testing and Sidak's post-test. (**E**) Quantitation of basal and H_2O_2-induced PAR levels in WT and *PARP1* KO cells via isotope dilution mass spectrometry (LC–MS/MS) using a previously published method (20). To induce PAR-formation, cells were treated with H_2O_2 as indicated. If indicated, cells were pretreated with 10 μM ABT888 for 45 min. Insert: Basal PAR levels in untreated WT and *PARP1* KO cells. Means ± SEM of $n = 3$ independent experiments. Statistical analysis was performed using one-way ANOVA testing and Sidak's post-test within one group of cells (i.e. WT, KO1, KO2). (**F**) LC–MS/MS analysis of PAR levels ± camptothecin (CPT) treatment for 30 min. Means of $n = 2$ independent experiments. R-Ado indicates ribosyl-adenosine.

crucial role in the response of cells to camptothecin (CPT) treatment (50,51). Using our highly sensitive LC–MS/MS technique, we analyzed if CPT treatment directly stimulates PARP activity in HeLa cells. As shown in Figure 1F, CPT treatment for 30 min led to a significant induction of PARP activity, yet this induction was far more moderate than after H_2O_2 treatment. Thus, a 1-μM treatment led to ∼2-fold and a 100-μM CPT treatment to 4-fold higher PAR levels compared to basal PAR levels in untreated cells. Importantly, this increase in PAR can be completely attributed to PARP1 activity, since no increase in PAR levels was observed in *PARP1* KO cells.

After having analyzed PAR metabolism in HeLa *PARP1* KO clones, we characterized cellular and functional consequences of the genetic deletion of *PARP1*. When culturing HeLa *PARP1* KO cells, it became apparent that these cells grew considerably slower compared to their WT counterparts. In agreement with this observation, proliferation analysis revealed that both *PARP1* KO clones showed significantly slower proliferation rates compared to WT, while the overall cell cycle distribution appeared to be unaffected (Figure 2A and B). A plethora of reports from *Parp1* KO mice and human cell culture studies using RNA interference and pharmacological inhibition of PARP activity showed that loss of PARP1 leads to a sensitization of cells towards genotoxic stimuli (31,32,52). To test if the same holds true in genetically-targeted HeLa *PARP1* KO cells, we performed a clonogenic survival analysis of HeLa WT and *PARP1* KO cells upon H_2O_2 treatment. Consistent with data from other mammalian systems, loss of PARP1 led to a significant sensitization of HeLa cells towards low-dose H_2O_2 treatment (Figure 2C). Next, we analyzed how PARP1 deficiency affects the response of HeLa cells to CPT treatment by performing cell viability and cell cycle analyses. Figure 2D demonstrates that HeLa *PARP1* KO clones were significantly sensitized to CPT treatment, resulting in lower cell viability two days after CPT treatment, which could be attributed to both increased apoptosis as well as necrosis rates. Interestingly, in terms of necrosis, the two independently generated *PARP1* KO clones showed significant differences, with clone KO2 showing higher necrosis induction than clone KO1. Such slight differences in the phenotypes of the two clones are not unexpected, since selection processes may occur during culturing of the clones, before initial biochemical analysis by immunofluorescence microscopy and Western blotting. To analyze if also nanomolar doses of CPT, which are assumed to induce primarily replicative stress without directly inducing DNA strand breaks, lead to a sensitization of *PARP1* KO cells, we performed a cell cycle analysis two days after CPT treatment (Figure 2E). These experiments revealed that CPT treatment caused a strong G2 arrest that was significantly increased in both *PARP1* KO clones. Since both *PARP1* KO clones showed similar properties, we focused on the usage of clone *PARP1* KO1 for further analyses.

In summary, we have generated a complete genetic knock-out of *PARP1* in HeLa cells in two independent clones. Furthermore, we provide a detailed characterization of these cells with regards to their PAR and NAD^+ metabolism, their growth characteristics, and their cellular responses after application of the genotoxins H_2O_2 and CPT.

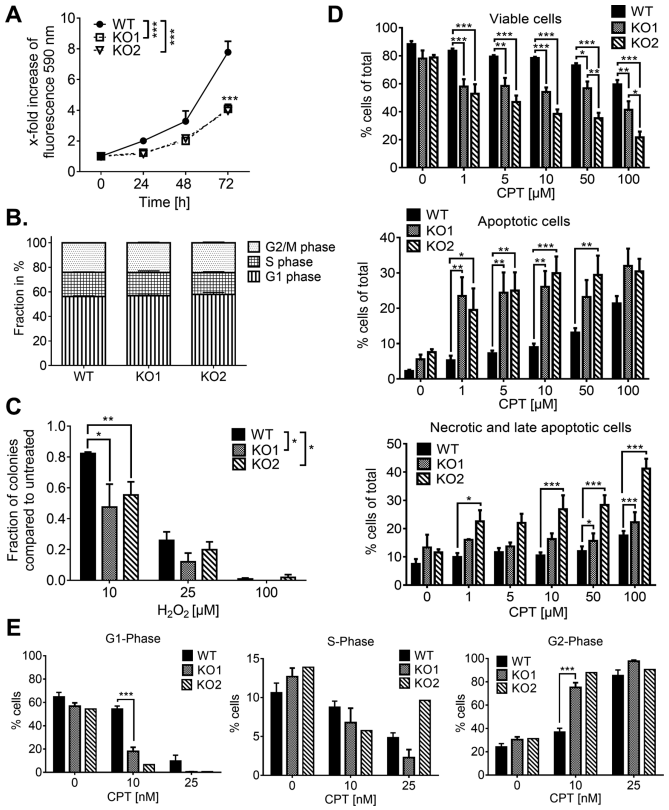

Figure 2. Functional consequences of *PARP1* deletion in HeLa cells. (**A**) Cell proliferation of HeLa WT and *PARP1* KO cells as analyzed by Alamar Blue assay for 3 days. Means ± SEM of $n = 3$ independent experiments. Statistical analysis was performed using two-way ANOVA testing and Sidak's post-test. (**B**) Cell cycle analysis of untreated WT and *PARP1* KO cells via PI staining and subsequent flow cytometric analysis. Means ± SEM of three independent experiments. (**C**) Clonogenic survival analysis. HeLa WT and *PARP1* KO cells were treated with H_2O_2 as indicated for 5 min and then plated and cultivated for 2 weeks prior to colony counting. Means ± SEM of $n = 3$ independent experiments. Statistical analysis using two-way ANOVA testing and Sidak's post-test. (**D**) Cytotoxicity analysis via annexin V/PI staining and subsequent flow cytometric analysis of HeLa WT and *PARP1* KO cells treated ± CPT in concentrations as indicated for 2 days. Viable cells refer to annexin V/PI-double negative cells (top); early apoptotic cells to annexin V-positive (middle), PI-negative cells; and necrotic and late-apoptotic cells to annexin V/PI-double positive cells (bottom). Ratios compared to total cell numbers. Means ± SEM of $n \geq 4$ independent experiments. Statistical analysis was performed using two-way ANOVA testing and Sidak's post-test. (**E**) Cell cycle analysis via PI staining and flow cytometric analysis 2 days after treatment of cells ± CPT in concentrations as indicated. Means ± SEM of $n \geq 4$ independent experiments except for data of *PARP1* KO2 cells; $n = 1$. Statistical analysis was performed using two-way ANOVA testing and Sidak's post-test.

Reconstitution of HeLa *PARP1* knock-out cells with PARP1 variants

By reconstituting HeLa *PARP1* KO cells with select PARP1 variants, we examined the cellular biochemistry of those. First, to exemplify the potential of this system for its usage in PARylation research, we analyzed two artificial PARP1 mutants that are of high interest to understand the cellular biochemistry of PARylation, i.e. a hypomorphic (E988K)

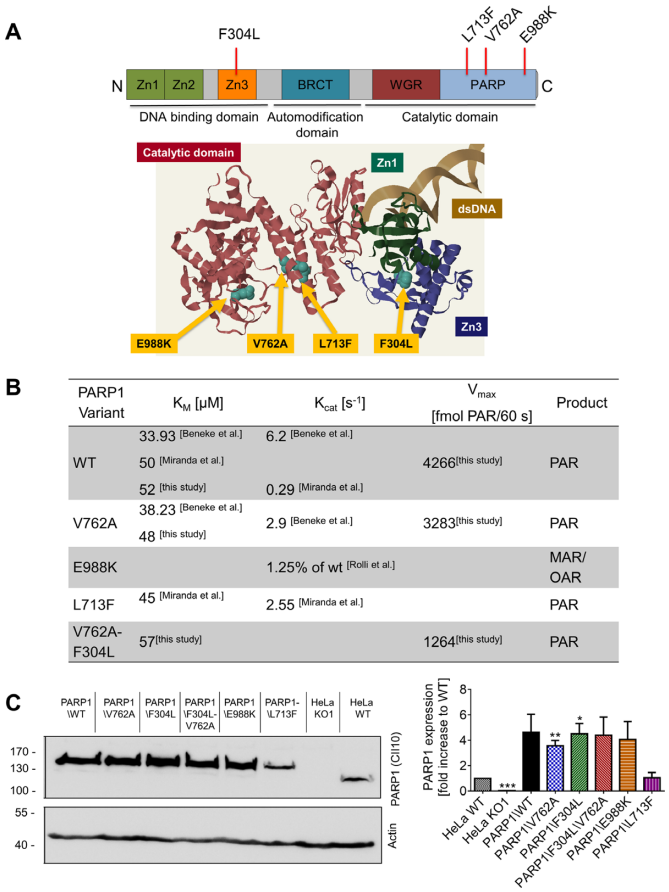

Figure 3. Overview of PARP1 variants included in this study. (**A**) PARP1 structure and localization of amino acid exchanges of PARP1 variants as used in this study. The 3D structure is in complex with a double-stranded DNA molecule [PDB code 4DQY (3)], without ZnF2 and WGR domains. (**B**) Biochemical parameters derived from rec. enzymes of the different PARP1 variants used in this study. Values were determined in the present study (*cf.* Figure 9) or taken from the literature as indicated. PAR indicates poly(ADP-ribose); MAR, mono(ADP-ribose); and OAR, oligo(ADP-ribose). (**C**) Western blot analysis of PARP1 protein levels in HeLa *PARP1* KO cells reconstituted with different PARP1-eGFP variants 2 days after transfection. Left: representative Western blot out of 4. Right: densitometric analysis of western blot signal intensities after normalization to transfection efficiencies. Means ± SEM of $n = 4$ independent experiments. Statistical analysis was performed using 1-sample *t*-test comparing the expression of the different PARP1-variants after transfection to endogenous PARP1\WT-levels in HeLa cells.

and a hypermorphic (L713F) PARP1 mutant (Figure 3A). Using a second set of PARP1 variants, we then analyzed biochemical and cellular properties of naturally occurring PARP1 variants, i.e. a PARP1 polymorphism that has been associated with increased risk for certain cancers (V762A) and a newly identified inherited PARP1 mutant in a patient with pediatric colorectal carcinoma (F304L) (Figure 3A). Figure 3B gives an overview of the biochemical parameters of the different variants as reported in the literature and the current study (see below). We generated eukaryotic expression constructs of the PARP1 variants using site-directed mutagenesis. To detect PARP1 expression in transfected HeLa cells and to monitor recruitment to sites of DNA damage, all variants were C-terminally tagged with eGFP. A transient-transfection approach was chosen to avoid potential counter-selection effects during cell culturing. As it is evident from Western blot (Figure 3C) and FACS analyses (Supplementary Figure S2), reconstitution of HeLa *PARP1* KO cells with these constructs led to a strong expression of the PARP1 variants, which was ∼4-5-fold higher than endogenous PARP1 expression in HeLa WT cells, with the exception of the PARP1\L713F variant, which showed per-cell expression levels comparable to WT cells. It is obvious that PARP1 protein levels may influence many cellular processes, although only weak correlations between PARP1 expression levels and PAR formation under non-stressed and upon genotoxic stress have been observed, indicating that PARP1 expression alone is not the limiting factor for PAR production (data not shown). In subsequent experiment, we included both HeLa WT cells as well as PARP1\WT-reconstituted cells as controls, which allows the assessment of any potential effects of PARP1 protein levels on functional outcomes.

Reconstitution of HeLa *PARP1* knock-out cells with wild-type and artificial PARP1 variants

In the first set of PARP1 mutants, we focused on a hypomorphic PARP1 mutant, with an aa exchange from glutamate to lysine at position 988 (E988K), and on a hypermorphic PARP1 mutant, with an aa exchange from leucine to phenylalanine at position 713 (L713F). Previously, PARP1\E988K was shown to exhibit mono- or oligo(ADP-ribosyl)ation activity in biochemical studies using recombinant enzymes (37,53,54) and its cellular behavior has been characterized by reconstituting mouse embryonic fibroblasts derived from *Parp1* knock-out mice (51,55). The PARP1\L713F mutant was originally identified as a gain-of-function mutant in a random mutagenesis screen and has been characterized on a biochemical level (3,56,57). Thus, this mutant mimics the effect of DNA-binding-induced distortions in the catalytic domain, thereby increasing PARP1 DNA-independent activity *in-vitro* up to 20-fold and elevating the catalytic efficiency of PARylation, while not affecting its affinity for NAD^+ (3) (Figure 3B). To the best of our knowledge, so far this variant has not been characterized in a cellular environment.

Cellular PAR and NAD^+ metabolism of artificial PARP1 mutants. To provide a basis for the analysis of cellular consequences of reconstituted HeLa *PARP1* KO cells, we conducted a detailed characterization of the cellular biochemistry of the different PARP1 variants with regards to PARylation and NAD^+ metabolism as well as PARP1 localization dynamics at sites of DNA damage. Using triple-color immuno-epifluorescence microscopy and image evaluation by an automated KNIME workflow, we examined the PARylation response upon treatment of PARP1-reconstituted cells with increasing doses of H_2O_2. As expected, PARP1-reconstituted cells showed a dose-dependent PAR formation (Figure 4A and B). The response was similar to the dose-response that had been observed in HeLa WT cells (Figure 1), however, in contrast to HeLa WT cells, saturation of PAR signals was reached already at a dose of 500 μM, presumably because of mod-

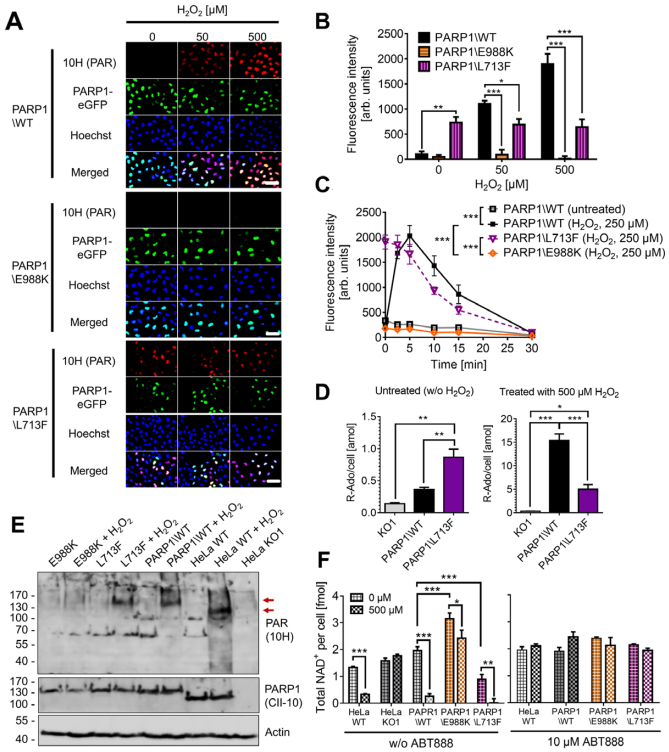

Figure 4. Cellular biochemistry of artificial PARP1 mutants. HeLa *PARP1* KO cells were transfected with eGFP-coupled constructs of PARP1, PARP1\L713F and PARP1\E988K. Analyses were performed 2 days after transfection. (**A**) Representative images from single cell immunoepifluorescence analysis of PARP1-eGFP and PAR after treatment of PARP1-reconstituted cells ± H_2O_2 as indicated for 5 min. Scale bars indicate 30 μm. (**B**) Densitometric analysis of imaging data as shown in (A). More than 100 cells were analyzed per experiment and condition in a semi-automated manner using a KNIME workflow. Means ± SEM of $n = 4$ independent experiments. Statistical analysis using matched two-way ANOVA testing and Sidak's post-test. (**C**) Time-course analysis of PAR levels in PARP1-reconstituted cells after treatment of cells with 250 μM H_2O_2. Means ± SEM of $n = 4$ independent experiments, >100 cells were analyzed per experiment and condition. Statistical analysis was performed using matched two-way ANOVA testing and Sidak's post-test. (**D**) LC–MS/MS analyses of PAR levels in *PARP1* KO1 cells and cells reconstituted with PARP1\WT and PARP1\L713F. Two days after transfection, cells were treated as indicated for 7 min. Levels were normalized to transfection efficiencies. Means ± SEM of $n = 3$ independent experiments. Statistical analysis was performed by one-way ANOVA testing and Tukey's post-test. (**E**) Western blot analysis of HeLa cell extracts of KO1 and PARP1-reconstituted cells, as indicated. 2 days after transfection, cells were treated with 500 μM H_2O_2 for 7 min. PARylated proteins were detected via the 10H antibody. Red arrows indicate the expected molecular weight of auto-PARylated PARP1. (**F**) NAD^+ levels in PARP1-reconstituted cells upon treatment ± H_2O_2 for 7 min as measured by an enzymatic NAD^+ cycling assay. Means ± SEM of $n = 3$ independent experiments, except for ABT888-treated samples, $n = 2$. Statistical analysis was performed using two-way ANOVA testing and Sidak's post-test.

erate PARP1 overexpression in reconstituted cells (Supplementary Figure S3). PARP1\E988K-reconstituted cells did not reveal any significant increase in PAR-derived fluorescent intensities (Figure 4A and B), which is in accordance to its described mono-/oligo-(ADP-ribosyl)ation activity (37,53,54). These results are in agreement with time-course analysis of PAR formation in PARP1-reconstituted cells upon H_2O_2 treatment, which revealed a transient PARylation response with peak levels of PAR formation at ∼5 min after treatment. Thirty minutes after H_2O_2 treatment, PAR levels returned to basal levels, due to the activity of PAR-degrading enzymes such as PARG (Figure 4C and Supplementary Figure S4). Furthermore, time-course analysis confirmed the inability of the PARP1\E988K variant to produce PAR (Supplementary Figure S4). On the other hand, cells reconstituted with PARP1\L713F produced PAR even in the absence of exogenous DNA damage, indicating that it is constitutively active not only in a cell-free system (3), but also in a cellular environment (Figure 4A and B). Interestingly, treating PARP1\L713F-reconstituted cells with H_2O_2 for 5 min did not lead to a further increase in PAR signal in IF analysis. Time-course analysis of H_2O_2-treated PARP1\L713F-reconstituted cells, however, revealed that 30 min after the genotoxic stimulus, PAR levels declined to basal levels as observed in untreated HeLa WT cells (Figure 4C), indicating that PARP1\L713 can still be stimulated by DNA damage presumably leading to a depletion of NAD^+. Validation of these results using isotope dilution mass spectrometry, confirmed that PARP1\L713 is constitutively active in cells, leading to 2.5-fold higher PAR levels in unstressed cells (Figure 4D). LC–MS/MS analysis also revealed that PAR levels in PARP1\WT-transfected cells increased by ∼43-fold after H_2O_2 treatment, while PAR levels of PARP1\L713F-transfected cells increased by ∼14-fold compared to unstimulated PARP1\WT- and ∼6-fold compared to unstimulated PARP1\L713F-transfected cells (Figure 4D). Comparison of LC–MS/MS and immunochemical analyses also demonstrate that immunofluorescence analysis can only give a semi-quantitative estimate of intracellular PAR levels, due to lack of sensitivity and the limited dynamic range for quantitation (20).

To test if constitutively active PARP1\L713F leads to PARP1 automodification, we performed western-blotting-based PAR detection using the 10H antibody. Figure 4E demonstrates that H_2O_2 treatment leads to PARP1 automodification in HeLa WT cells as well as in PARP1\WT-reconstituted HeLa *PARP1* KO1 cells (indicated by red arrows). As expected, H_2O_2 treatment of E988K-reconstituted cells did not result in a significant increase in PAR signal intensity. In agreement with IF and LC–MS/MS analyses, H_2O_2 treatment triggered PARylation and PARP1 automodification in PARP1\L713F-reconstituted cells. However, no PARP1 automodification could be observed in untreated cells, suggesting that constitutive activity of PARP1\L713F mainly produces PAR attached to other proteins than PARP1 or not covalently bound to proteins at all.

To obtain further insight into the activities of PARP1 variants in reconstituted cells, we analyzed NAD^+ levels in untreated as well as in H_2O_2- and PARP inhibitor-treated cells. Transfection efficiencies of individual samples were determined in parallel via flow cytometry and have been taken into account in Figure 4F. These experiments confirmed that, as expected, cells reconstituted with PARP1\WT for two days responded similar as HeLa WT cells by showing a drastic drop in NAD^+ levels upon H_2O_2 treatment, which could be completely inhibited by ABT888 (Figure 4F). Unexpectedly, cells that had been reconstituted with PARP1\E988K, displayed a significant increase in total NAD^+ amounts per cell compared to PARP1\WT-

reconstituted cells. Furthermore, H_2O_2 treatment led to a moderate, but statistically significant, drop in NAD^+ levels, which is consistent with the fact that the PARP1\E988K mutant acts as a mono- or oligo-(ADP-ribose) transferase, which is incapable to form PAR chains that can be recognized by the 10H antibody. Strikingly, the increase in NAD^+ levels in PARP1\E988K-reconstituted cells could be completely inhibited by PARP inhibitor treatment (Figure 4F), suggesting that the mono- or oligo(ADP-ribosyl)ation activity of PARP1\E988K is responsible for the effect observed. Consistent with our PARylation analysis, NAD^+ levels in PARP1\L713F-reconstituted cells were reduced by >40% under basal conditions and showed a total exhaustion in H_2O_2-treated cells, which could be completely abolished by PARP inhibitor treatment.

In summary, these results demonstrate that single aa exchanges within PARP1 can cause dramatic effects on PARP1's enzymatic activity and NAD^+ metabolism in a cellular environment. This holds true for both (i) a hypomorphic exchange, such as E988K, thereby generating a mono- or oligo(ADP-ribosyl) transferase, or (ii) a hypermorphic exchange, such as L713F, thereby generating a constitutively active PARP1 variant, whose enzymatic activity is partially uncoupled from its DNA binding ability and mediates the synthesis of mainly free PAR in cells under non-stressed conditions.

Recruitment dynamics of artificial PARP1 mutants to DNA damage. Since enzymatic PARP1 activation is in many cases directly related to its DNA binding status, we analyzed the spatio-temporal dynamics of recruitment of PARP1-eGFP to DNA damage sites induced by multi-photon irradiation in the infrared spectrum (58,59). For PARP1\WT, we observed a fast and strong recruitment to sites of DNA damage reaching its maximum level 1 min after damage induction and decreasing progressively thereafter (Figure 5A and B). This is consistent with what has been observed previously in other cellular systems (55,60). For PARP1\E988K the maximum level of recruitment was reduce by 50% as compared to WT. Interestingly, this level remained unchanged over a period of 6 min after laser-induced damage. Thus, in contrast to PARP1\WT, there was no decrease of PARP1/E988K at the damage site during the time of experimental observation. These results are largely consistent with the binding dynamics of PARP1\E988K at UV-irradiated sites reported in a mouse system (55). Recruitment experiments using the constitutively active mutant PARP1\L713F revealed a similar overall behavior of this mutant as compared to PARP1\WT, with a moderate, but significant reduction in the maximum level of recruited protein. Altogether, these data demonstrate that the dynamics of PARP1 recruitment at micro-irradiated sites is strongly affected by the protein's activity.

Non-covalent PARP1–PAR interaction. In many instances, recruitment of DNA repair factors is mediated by non-covalent PAR-protein interactions (19). The recruitment kinetics of PARP1\E998K as observed in the current study and by (55) suggest that non-covalent binding to locally formed PAR may affect PARP1 binding to sites of DNA damage. Non-covalent PARP1–PAR interaction may lead to conformational changes within the secondary and tertiary structure of PARP1, thereby regulating its binding to DNA. Previously studies reported non-covalent PARP1–PAR interaction (18,61,62). Thus, using a peptide array-approach, Chapman *et al.* reported a multitude of potential PAR binding sites within the PARP1 protein sequence (18). Moreover, Huambachano *et al.* reported PAR binding to the ZnF2 and a C-terminal region of PARP1, i.e. dsDNA binding domain (62), but in the latter case the binding site has never been specified. To the best of our knowledge, a comprehensive characterization of PAR binding to full-length PARP1 has not been reported so far. Therefore, we tested if PARP1 and PAR interact non-covalently, which could lead to an accumulation of PARP1 molecules at sites of DNA damage. To this end, we used three different biochemical approaches to characterize the non-covalent interaction of PAR with full length rec. PARP1. (i) We performed Western blotting of rec. PARP1, incubated membranes in the presence or absence of *in-vitro* synthesized PAR, and detected bound PAR under high-stringency conditions. Figure 6A demonstrates that PARP1 interacts with PAR non-covalently. (ii) This result was further confirmed by immuno-slot blotting (Figure 6B). Both methods analyze binding of PAR to rec. PARP1 immobilized on a membrane. (iii) To analyze PARP1–PAR interaction in solution, we performed a modified EMSA using biotin-end-labelled PAR of defined chain length as a bait. We observed the formation of three defined macromolecular complexes further confirming that PARP1 interacts with PAR in a non-covalent manner (Figure 6C). In general, non-covalent PAR-protein binding can be mediated by several different PAR binding modules (19).

The most abundant one within the human proteome is the PAR binding motif (PBM), which comprises a weakly conserved consensus sequence containing a basic/hydrophobic core helix. Using a previously published target sequence (41,42), we searched for putative PBMs within the PARP1 aa sequence and identified two potential binding sites within ZnF2 and ZnF3, respectively (Figure 6D). No PBM has been identified in the C-terminal region of PARP1. [N.B. As stated above, it is important to note that the molecular basis of the PARP1–PAR interaction is probably highly complex and other binding sites as shown by (18,62) presumably contribute to non-covalent PARP1–PAR interaction.] To test if these aa sequences mediate PAR binding *in vitro*, we used membrane-immobilized peptides (PepSpot approach) in a PAR overlay assay. PBM1 showed a strong and PBM2 a weak PAR binding (Figure 6E), which could be completely abolished by exchanging critical lysines with alanines.

Next, we were interested in potential functional consequences of the PARP1–PAR interaction. Based on the presence of a PBM within ZnF2, we speculated that the non-covalent PARP1–PAR interaction could directly affect the ability of PARP1 to bind to DNA. To test this hypothesis, we performed EMSAs of PARP1-DNA complexes formed in the presence or absence of PAR. These results show that PARP1 binds to this DNA substrate in a dose-dependent manner and, importantly, this binding could be already inhibited by the presence of PAR in a molar ratio as low as 1:10 (PAR:PARP1) (Figure 6F).

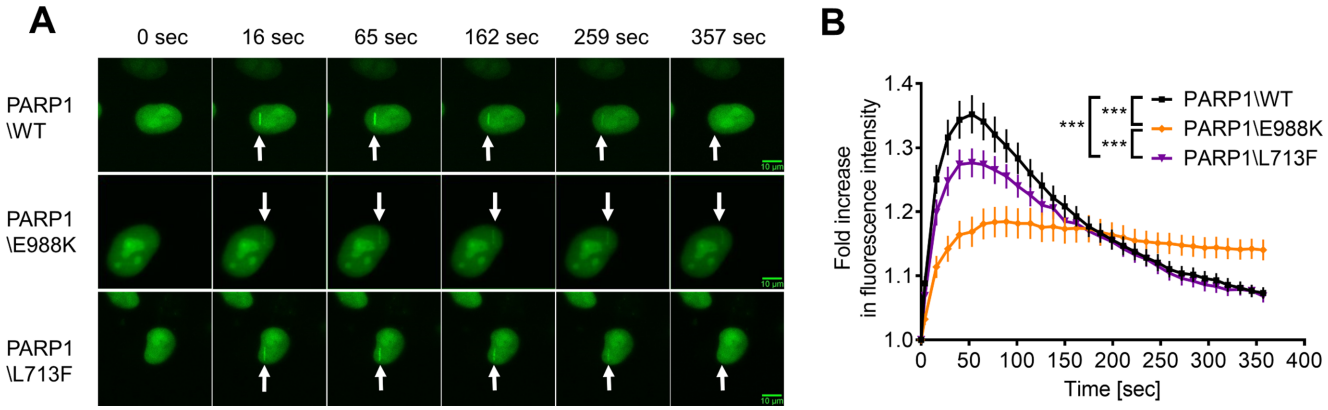

Figure 5. Recruitment and dissociation kinetics of PARP1-eGFP at sites of laser-induced DNA damage. (**A**) Representative imaging data. Scale bars indicate 10 μm. (**B**) Densitometric quantitation of signal intensities from imaging data as shown in (A). Means ± SEM of $n = 3$ independent experiments, >29 cells were analyzed per experiment and condition. Statistical analysis was performed using two-way ANOVA testing and Sidak's post-test.

In summary, these results demonstrate that PARP1 activity is necessary for the efficient recruitment to as well as release from sites of laser-induced DNA damage. Furthermore, direct non-covalent PARP1–PAR interaction can contribute to these effects by (i) efficiently attracting PARP1 molecules to sites of active PARylation and (ii) subsequently regulating the release of highly modified PARP1 molecules from DNA.

Cellular consequences of PARP1 reconstitution. Having analyzed the cellular biochemistry of the PARP1\E988K and PARP1\L713F mutants in the absence of any potentially interfering endogenous PARP1\WT, we examined potential cellular consequences of the altered PARylation metabolism in PARP1-reconstituted cells. PARP1\E988K-reconstituted cells showed considerable alterations in cellular morphology. Thus, we observed that PARP1\E988K expression induced significant changes in flow cytometric dot-blots. Forward (FSC) and side scatter (SSC) intensities were significantly increased (Supplementary Figure S5A). Furthermore, when we quantified the areas of nuclei from epi-fluorescence microscopic images of reconstituted cells, we observed that nuclei of PARP1\E988K-reconstituted cells were ∼50% enlarged compared to PARP1\WT, *PARP1* KO and other PARP1-reconstituted cells (Supplementary Figure S5B). In addition, 3D deconvolution microscopy of Hoechst33342-labeling revealed signs of altered nuclear architecture of PARP1\E988K-expressing cells as compared to PARP1\WT. Thus, nucleoli of PARP1\E988K-reconstituted cells appeared enlarged and surrounded by compacted perinucleolar heterochromatin (Supplementary Figure S5C).

While we could not observe any significant changes for the chromatin markers H3K27me3 and H3K4me3 in PARP1-reconstituted cells (data not shown), another cause for differences in nuclear sizes may be alterations in cell cycle regulation (63). To test if PARP1\E988K reconstitution led to alterations in cell cycle distribution, we analyzed the cell cycle status of reconstituted cells via PI staining and flow cytometric analysis. While expression of the PARP1\L713F mutant only slightly influenced the HeLa cell cycle without application of additional stress, expression of the PARP1\E988K mutant induced a strong G2 arrest three days after transfection (Figure 7A). Importantly, PARP inhibitor treatment of PARP1-reconstituted cells did not affect the cell cycle status at all, but, remarkably, rescued the cell cycle defect of PARP1\E988K-expressing cells completely. These results are consistent with our analysis of the NAD^+ status in PARP1\E988K-reconstituted cells and indicate an active role of mono- or oligo(ADP-ribosyl)ation in inducing the observed effects. Typically, a G2 arrest in cell cycle progression can be caused by accumulating DNA damage. To test if PARP1\E988K expression leads to a DNA damage response, we analyzed several key factors of DNA damage signaling in PARP1-reconstituted cells, such as phosphorylated p53 at serine 15 (ph-p53), γH2A.X, and p16 (Figure 7B). Western blot analysis revealed that PARP1\L713F-expressing cells showed slightly enhanced γH2A.X levels, whereas PARP1\E988K-expressing cells exhibited a robust increase in γH2A.X and ph-p53 staining two days after transfection, while p16 expression was not affected in cells expressing PARP1 mutants. As expected, PARP inhibition by ABT888 also induced γH2A.X levels in HeLa WT and PARP1\WT-reconstituted cells (Figure 7C). However, unexpectedly, PARP inhibition in PARP1\E988K-reconstituted cells led to reduced γH2A.X levels, indicating that DNA damage induction in PARP1\E988K-reconstituted cells is mediated by residual mono- or oligo-(ADP-ribosyl)ation activity of the PARP1\E988K mutant and not due to a potential PARP1 trapping effect. The increase in nuclei size, G2 arrest and increased levels of γH2A.X observed for PARP1\E988K-reconstituted cells is reminiscent of replicative stress, as previously observed in hydroxyurea-treated cells (64). Of note, PARP1\E988K-reconstitued cells showed increased levels of the replicative stress marker phRPA2 (Ser 4/8), which can be mitigated by PARP inhibitor treatment (Figure 7D), suggesting that the observed phenotype is directly induced by residual PARP1\E988K activity rather than a trapping effect of PARP1\E988K at sites of DNA damage. In support of the toxic effect of PARP1\L713F expression is the finding that PARP inhibitor treatment led to a considerable increase in

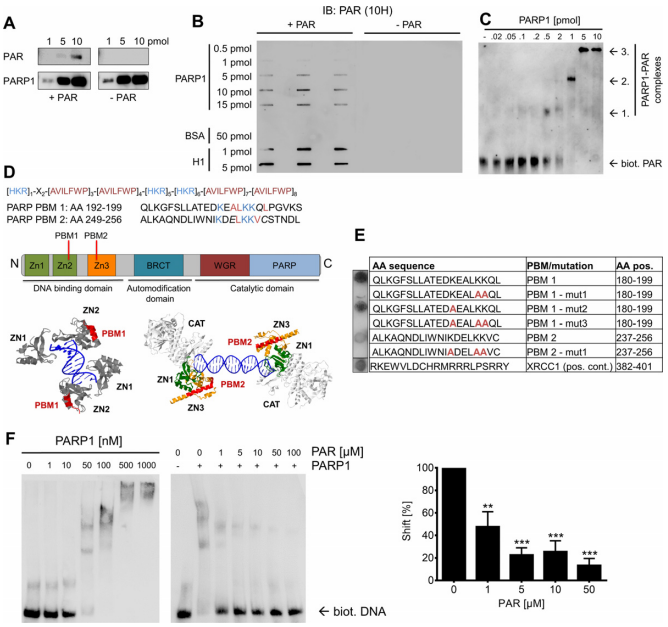

Figure 6. Non-covalent PARP1–PAR interaction. (**A**) Analysis of PARP1–PAR interaction by PAR overlay assay using increasing amounts of recombinant PARP1 as indicated. After protein transfer, membranes were incubated with (left panel) or without (right panel) purified PAR (0.2 μM). PAR binding was detected using the 10H antibody after high-stringency washing to remove non-specifically bound PAR. (**B**) Immuno slot-blot PAR binding assay using increasing amounts of recombinant PARP1. Membranes were incubated with PAR (0.2 μM) and bound PAR was detected using the 10H antibody after high-stringency washing. (**C**) Analysis of PARP1–PAR interaction in solution using a modified PAR-EMSA. End-biotinylated PAR of defined chain length (30–35 mer, 0.5 pmol ADP-ribose) was incubated with recombinant PARP1. PARP1–PAR binding was assessed by native TBE gel electrophoreses and Western blotting. Three distinct complexes (1–3) were formed in a PARP1-dependent manner. (**D**) *Upper panel. In silico* search for putative PAR-binding sites within the PARP1 sequence using the search sequence displayed at the top of the panel. Two potential PAR binding motives (PBMs), i.e. PBM1 (1 mismatch) and PBM2 (two mismatches), were identified in Zn2 and Zn3, respectively. *Lower panels.* Localization of PBM1 and PBM2 within Zn2 and Zn3, respectively. Structures based on PDB codes 4AV1 and 4DQY (3). (**E**) PAR binding ability of peptides comprising aa sequences of PBM1/2 and peptides comprising aa exchanges potentially responsible of PBM-PAR interactions using a PepSpot analysis. 'AA pos.' indicates aa positions within full-length PARP1 sequence (85). A peptide sequence derived from a PBM in XRCC1 served as a positive control. (**F**) DNA-PARP1 EMSA using a known biotinylated double-stranded DNA oligonucleotide (200 fmol). *Left*. DNA-PARP1 interaction in the absence of PAR. *Middle*. Rec. PARP1 (100 nM) was incubated with increasing concentrations of PAR as indicated. *Right*. Densitometric evaluation of EMSAs. Means ± SEM of n = 3 independent experiments. Statistical analysis was performed using 1-way ANOVA testing and Sidak's post-test.

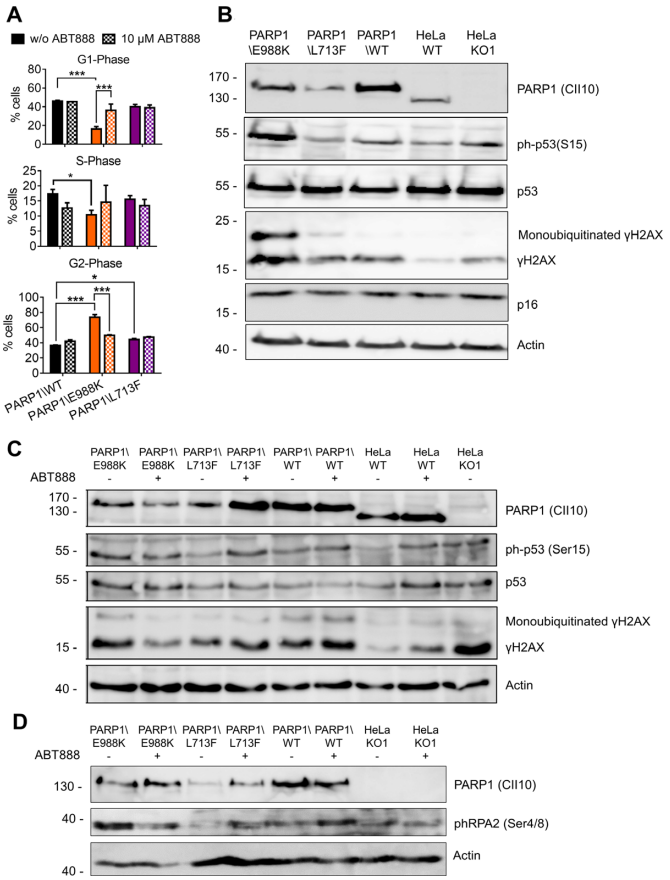

Figure 7. PARP1\E988K affects cell cycle regulation and induces DNA damage signaling. (**A**) Cell cycle analysis by PI staining and subsequent flow cytometric analysis 3 days after transfection of HeLa *PARP1* KO cells reconstituted with PARP1\WT, PARP1\E988K and PARP1\L713F. PARP1\E988K induces a G2 arrest, which can be rescued by treating cells with 10 μM ABT888. Means ± SEM of $n = 6$ independent experiments, except of ABT888-treated samples, $n = 2$. Statistical analysis was performed using two-way ANOVA testing and Sidak's post-test. (**B**) Analysis of DNA damage response markers, i.e. phospho-S15-p53, γH2A.X and p16 in WT, *PARP1* KO and PARP1-reconstituted cells as indicated 2 days after transfection. Cells reconstituted with PARP1\E988K displayed increased phospho-S15-p53 and γH2A.X levels and cells reconstituted with PARP1\L713F showed slightly elevated γH2A.X levels. Immunochemical detection of PARP1, p53 and actin served as controls. Shown is a representative experiment out of three. (**C**) Western blot analysis of ph-p53 and γH2A.X levels in PARP1-reconstituted cells (±10-μM ABT888 treatment). (**D**) Western blot analysis of the replicative stress marker phospho-RPA2 (Ser4/8) in PARP1-reconstituted cells (±10-μM ABT888 treatment). Immunochemical detection of PARP1 and actin served as controls.

PARP1\L713F expression in *PARP1* KO cells (Figure 7C and D).

Since PARP1\E988K-expressing cells entered a G2 arrest, we assumed that expression of this variant could induce cell death in HeLa cells. We analyzed cell viability via annexin V/PI staining three days after transfection. Cells overexpressing PARP1/WT showed comparable viability as HeLa WT cells (compare Figures 2 and 8). Consistent with a G2 arrest, PARP1\E988K-expressing cells showed a higher rate of early as well as late apoptotic/necrotic cells compared to PARP1\WT-reconstituted cells, at a similar level compared to HeLa *PARP1* KO cells transfected with a plasmid carrying GFP only (i.e. labeled with GFP-cont in Figure 8A). More strikingly, however, expression of PARP1\L713F in HeLa *PARP1* KO cells revealed to be highly cytotoxic reducing viability from 80% for PARP1\WT-reconstituted cells to ∼40–50% for PARP1\L713F-reconstituted cells (Figure 8A). Most of this effect could be attributed to annexin V-positive, but PI-negative cells indicating that high basal PAR levels in these cells could drive cells into apoptosis without any obvious induction of cell cycle arrest in viable cells (at least under the conditions tested). Interestingly, pretreatment with the

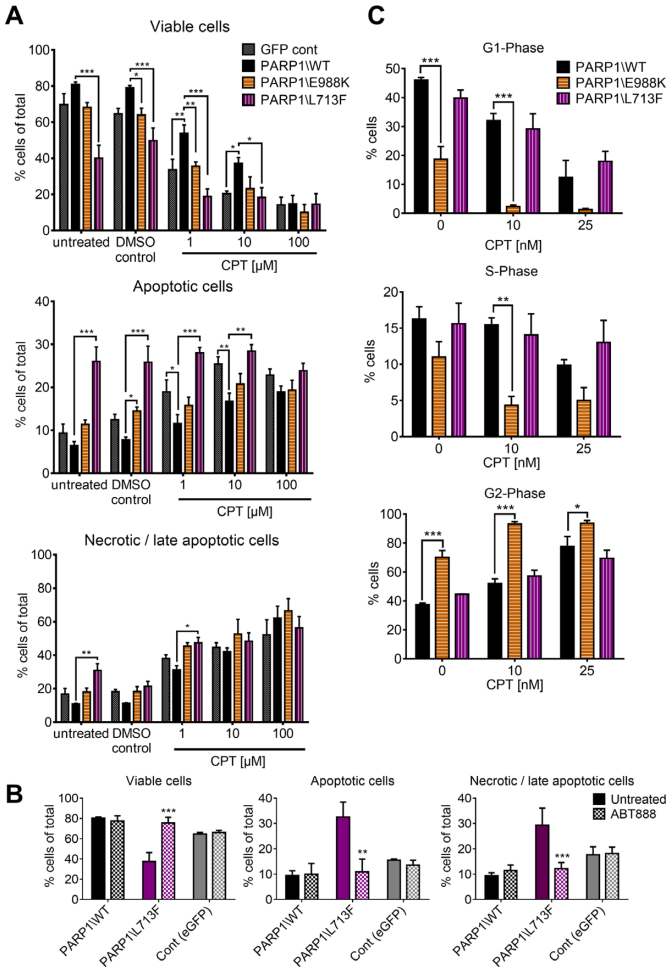

Figure 8. PARP1 mutants influence cell viability and cell cycle progression upon CPT treatment. (**A** and **B**) Analysis of viable, apoptotic and necrotic cells 3 days after transfection of HeLa *PARP1* KO cells reconstituted with PARP1, PARP1\E988K, and PARP1\L713F by annexinV / PI staining and subsequent flow cytometric analysis. GFP cont indicates cells transfected with a plasmid carrying only GFP. Cells were treated (**A**) with CPT in concentrations as indicated 24 h after transfection or (**B**) with 10 μM ABT888 directly after transfection. Viable cells refer to annexin V/PI-double negative cells; (early) apoptotic cells to annexin V-positive, PI-negative cells; and necrotic and late-apoptotic cells to annexin V/PI-double positive cells (ratios compared to total cell numbers). Means ± SEM of $n \geq 3$ independent experiments. Statistical analysis was performed using two-way ANOVA testing and Sidak's post-test. (**C**) Cell cycle analysis of PARP1-reconstituted cells as indicated 3 days after transfection and 2 days after CPT treatment via PI staining and subsequent flow cytometric analysis. Means ± SEM of $n = 3$ independent experiments. Statistical analysis was performed using two-way ANOVA testing and Sidak's post-test.

pharmacological PARP inhibitor ABT888 was able to mitigate the induction of early apoptosis, indicating, that not the PARP1\L713F protein itself, but the constitutive activity of this variant is responsible for the increased apoptosis rate (Figure 8B). Since the loss of PARP1 in HeLa cells led to a significant sensitization towards CPT treatment, we examined if PARP1-reconstitution could rescue this effect. Indeed, when treating cells with increasing doses of CPT two days prior to analysis, PARP1\WT reconstitution could significantly rescue the sensitization effect observed in *PARP1* KO cells (Figure 8A). Interestingly, neither reconstitution with PARP1\E988K nor with PARP1\L713F were able to rescue the *PARP1* KO effect, indicating that full PARP1 functionality is necessary to protect cells from CPT-induced genotoxic stress. Furthermore, CPT-induced cell death could be mostly attributed to the induction of necrotic cell death, while apoptosis was only slightly induced in PARP1\WT and PARP1\E988K-reconstituted cells and stayed at a constant high level in PARP1\L713F-reconstituted cells (Figure 8A). Consistent with these results, treatment of PARP1-reconstituted cells with CPT in the low nM range, led to a G2 arrest for all three variants, but with the highest proportion for PARP1\E988K-reconstituted cells (Figure 8C).

It has been reported that PAR could induce the release of apoptosis inducing factor (AIF) from mitochondria and induce apoptosis via a pathway called parthanatos (65,66). To examine whether this mechanism contributes to cell death in unchallenged PARP1\L713F-reconstituted cells, we used immunofluorescence confocal microscopy to analyze subcellular AIF distribution. Although cells reconstituted with the PARP1\L713F variant exhibited changes in the non-nuclear AIF distribution compared to PARP1\WT- reconstituted cells, no nuclear translocation of AIF has been observed (Supplementary Figure S6). Although at this stage, we cannot exclude that the amount of AIF in the nucleus is below the technical detection limit, it is unlikely that cell death triggered by PARP1\L713F expression is mediated by AIF translocation. Presumably, PARP1\L713F-mediated cell death is a result of depletion of cellular NAD^+ pools (Figure 4F) or through inhibition of glycolysis (67,68).

In summary, modulating PARylation metabolism led to remarkable cellular consequences, such as higher apoptosis rates induced by increased basal PAR levels through expression of the constitutively active PARP1\L713F mutant, or severe effects on cell cycle progression by expression of the mono/oligo(ADP-ribosyl) transferase PARP1\E988K. Importantly, in both cases effects were mediated by enzymatic activities of the PARP1 mutants, since they could be blocked by PARP inhibition.

Reconstitution of HeLa *PARP1* knock-out cells with natural PARP1 variants

In a second set of PARP1 variants, we analyzed two variants naturally occurring in humans, i.e. (i) the V762A polymorphic variant (valine to alanine exchange at aa position 762) (35). This variant displays reduced enzymatic activity in *in vitro* studies using rec. PARP1 (36,37) and is associated with higher risks for specific types of tumors in certain ethnicities (38,39). To the best of our knowledge, PARP1\V762A has not been characterized in detail in a cellular environment. (ii) Using exome sequencing of peripheral blood DNA from a patient with pediatric colorectal cancer, we identified the V762A polymorphism to co-occur with a novel rare *PARP1* mutation, i.e. a genomic 910T>C mutation leading to a phenylalanine to leucine exchange at the protein level at aa position 304, i.e. F304L. This mutation was maternally inherited. Importantly, although not in the focus of the present study, the paternal

family history of this patient was positive for breast and ovarian cancer, which can be explained by an accompanying pathogenic frameshift mutation c.2808_2811del (p.A938fs) in the *BRCA2* gene [MIM 600185]. This aberration was found to be present in the proband as well. Predisposition to pediatric CRC in *BRCA2* mutation carriers has not been reported before, but germline biallelic *BRCA2* mutations cause Fanconi anemia, a condition that predisposes to pediatric cancer (69). We therefore assessed this patient for the presence of a second germline mutation in *BRCA2*, which was not found. Subsequent whole exome sequencing revealed no *de novo* mutations, nor mutations affecting both alleles of one gene. The c.910T>C (p.F304L) variant in the *PARP1* gene (Figure 9A), which was one of the rare candidate pathogenic variants, was analyzed in more detail in tumor tissue-derived DNA of this patient. Of the chromosome 1q42.12 region, which harbors *PARP1*, two copies were present, and SNP array data revealed no indication for acquired uniparental disomy of this region in the tumor tissue. After Sanger sequencing of *PARP1* on tumor DNA no second hit mutation was found. The F304 residue of PARP1 is a highly conserved residue at the homodimer interface within the third zinc-binding domain, which may be important for PARP1 dimerization and DNA-dependent enzyme activation (70). At present it is unclear if this *PARP1* mutation may have contributed to colon carcinogenesis. To address this hypothesis, we first examined if the F304L exchange disturbs PARP1 enzymatic activity. To this end, we generated mutant *PARP1* cDNAs by site-directed mutagenesis, coding for either a phenylalanine or leucine at position 304 and either a valine or alanine at position 762. Activity testing of rec. proteins carrying the four different combinations was performed by a well-established biochemical immuno-slot blot assay (Supplementary Figure S7). This confirmed previous results showing that the V762A exchange is associated with reduced PARP1 activity (Figure 9B). Importantly, the PARP1\F304L variant showed reduced PARP1 activity by about 50% compared to respective WT, both in the absence and presence of the V762A polymorphism (Figure 9B). Of note, PARP1\F304L\V762A - as found in the patient - exhibited only 30% of the maximum activity compared to PARP1\WT. These results indicate that the presence of both the F304L and V762A amino acid exchanges in PARP1 in the patient resulted in a cumulative reduction in enzymatic activities.

Next, we analyzed the cellular properties of these two natural PARP1 variants. This paves the way towards a molecular risk assessment also of other natural occurring PARP1 variants to assess the risk of carriers of these variants for disease development. Figure 9C shows that the enzymatic activities of the different natural PARP1 variants behave very similar in a cellular environment compared to the *in vitro* setting as shown in Figure 9B. Thus, when reconstituting HeLa *PARP1* KO cells with the different natural PARP1 variants, treating them with 50 μM H_2O_2, and subsequently analyzing their PAR forming ability via immuno-epifluorescence microscopy, PAR formation was reduced by ∼31% and ∼42% in cells reconstituted with the PARP1\V762A and PARP1\F304L variants, respectively (Figure 9C). Strikingly, under those conditions the activity of the PARP1\V762A\F304L variant declined by ∼57%

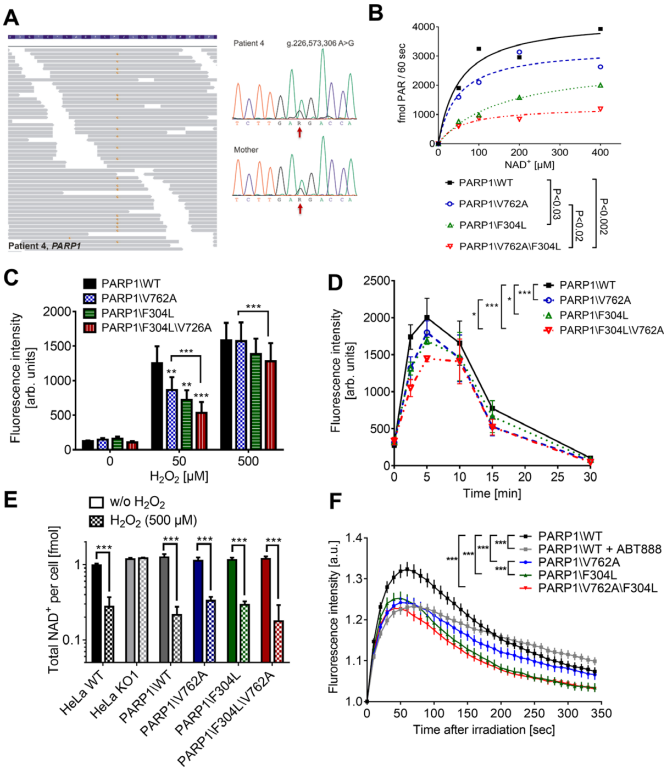

Figure 9. Biochemical and cellular characteristics of natural PARP1 variants. (**A**) An inherited *PARP1* mutation identified by exome sequencing in a patient with pediatric colorectal cancer. The panel on the *left* shows a subset of the sequencing reads spanning the individual mutations (data based on hg19); the panel on the *right* shows the validation by Sanger sequencing in the child and the maternal samples to indicate the mode of inheritance. Position of the mutation is indicated by red arrows. (**B**) Biochemical characterization of natural PARP1 variants as used in this study. Rec. enzymes were expressed in the *Sf*9/baculovirus system and purified via size exclusion and affinity chromatography. PARP1 activity was examined by incubating 5 nM PARP1 with increasing concentrations of NAD^+ as indicated in a reaction mixture as described in material and methods section. Afterward, 15% of reaction mixtures were slot-blotted on a nylon membrane (see Supplementary Figure S7) and PAR content was analyzed by immunochemical staining using the 10H antibody. Means of n = 3 independent experiments. A non-linear Michaelis-Menten model was used for curve fit. Statistical analysis using 2-way ANOVA testing. (**C**) Analysis of intracellular PARP1 activity in *PARP1* KO cells reconstituted with PARP1 variants as indicated 2 days after transfection by immuno-epifluorescence microscopy as shown in Figure 4 (for representative raw data refer to Supplementary Figure S7). Cells were treated with H_2O_2 for 5 min in concentrations as indicated, and PAR levels of eGFP-positive cells were examined using the anti-PAR-specific mAB 10H. Means ± SEM of $n = 5$ independent experiments. Statistical analysis was performed using matched two-way ANOVA testing and Sidak's post-test. (**D**) Time-course analysis of PAR formation in PARP1-reconstituted cells after treatment of cells with 250 μM H_2O_2. Means ± SEM of $n = 4$ independent experiments (>100 cells per experiment). Statistical analysis using matched two-way ANOVA testing and Sidak's post-test. (**E**) NAD^+ levels in WT, *PARP1* KO and PARP1-reconstituted cells ± H_2O_2 treatment for 7 min as evaluated by an enzymatic NAD^+ cycling assay. Means ± SEM of $n = 3$ independent experiments. Statistical analysis was performed via 2-way ANOVA testing and Sidak's post-test. (**F**) Recruitment and dissociation kinetics of natural PARP1 variants at sites of laser-induced DNA damage. For representative raw data refer to Supplementary Figure S7. Means ± SEM. Evaluation from ≥35 cells from three independent experiments. Statistical analysis was performed using two-way ANOVA testing and Sidak's post-test.

compared to PARP1\WT. Treatment of cells with higher doses of H_2O_2 (500 μM) resulted in more moderate differences in PAR formation, with a ∼20%-reduced PAR formation for the PARP1\V762A\F304L variant compared to PARP1\WT (Figure 9C). This indicates that the maximum PAR forming ability in a cellular environment is similar for the different variants, since under such treatment conditions with high concentrations of H_2O_2, the PAR formation in the cellular system is already saturated (Supplementary Figure S3). Consistent with results from the dose-response analysis, also time-course studies revealed reduced activities for the PARP1\V762A and the PARP1\F304L variants (Figure 9D). NAD^+ levels in cells reconstituted with the different natural PARP1 variants revealed no differences under non-stress conditions and only minor differences after challenging cells with H_2O_2 (Figure 9E). This suggests that PARP1 variants still keep their NAD^+ hydrolyzing (NADase) function (71) active, which is consistent with the findings of similar K_m values of the different variants (Figure 3B). In a next step, we tested if the aa exchanges of the natural PARP1 variants influence their localization dynamics at sites of DNA damage by monitoring the localization of fluorescently labeled PARP1 variants at site of laser irradiation as described above (Figure 9F and Supplementary Figure S8). Interestingly, PARP1\WT-reconstituted cells that were treated with ABT888 shortly before irradiation, behaved similarly to the PARP1\E988K mutant, i.e. reduced maximum levels of recruitment, but longer persistence at the site of the damage (Figure 5B). When analyzing cells reconstituted with the different natural PARP1 variants, it became evident that all variants showed strongly reduced recruitment to sites of laser damage with the strongest effects observed for the PARP1\V762A\F304L variant (Figure 9F and Supplementary Figure S8). Interestingly, while the maximum protein levels at sites of laser damage were quite similar for both the PARP1\V762A and the PARP1\F304L variant, the dissociation behavior was significantly different, since the PARP1\V762A variant persisted longer at sites of laser-damage than PARP1\F304L.

In summary, we have identified a novel PARP1 mutant (i.e. PARP1\F304L\V762A) in a patient with pediatric colorectal carcinoma and provide a biochemical characterization of enzymatic properties of this variant. Furthermore, cellular analyses of PARP1\F304L, PARP1\V762A, PARP1\F304L\V762A revealed significant alterations in their enzymatic activities and localization dynamics at sites of DNA damage that might contribute to a higher risk of disease development.

DISCUSSION

There is a lack of systems with a complete genetic deletion of *PARP1* in a human setting. Recently, gene editing technologies have become commonly available, such as TALEN or CRISPR/Cas technologies, which allow genetic modification in human cancer cell lines. Here we used the TALEN technology to generate a complete genetic deletion of *PARP1* in one of the most widely used human cell culture systems, i.e. HeLa cells. We comprehensively characterized such HeLa *PARP1* KO cells with regards to their PARylation metabolism and stress response phenotype. Furthermore, we used this system to test a spectrum of artificial and natural human PARP1 variants in a cellular environment without interference of endogenously expressed PARP1 to improve our understanding on the cellular biochemistry and functions of PARP1.

HeLa *PARP1* KO cells did not express detectable levels of PARP1 nor did they reveal any H_2O_2-induced PARP activity, when analyzing intracellular NAD^+ levels or using the 10H antibody in immunofluorescence microscopy (Figure 1). This suggests that in HeLa cells, PARP1 is responsible for most of the genotoxic stress-induced PARylation and that PARP2 only plays a minor role in this cell type. Ame *et al.* showed that 3T3 fibroblasts derived from *Parp1* KO mice still produce significant amounts of PAR after H_2O_2 treatment (as evaluated by 10H-immunofluorescence microscopy), which led to the discovery of *Parp2* (72). Using highly sensitive isotope dilution LC–MS/MS (20), we did indeed observe low-level induction of PARylation upon H_2O_2 treatment (Figure 1), which is consistent with the notion that PARP2 can in part compensate the loss of PARP1 also in HeLa cells. Strikingly, basal levels of PAR were not affected at all in HeLa *PARP1* KO cells, demonstrating that under unstressed conditions other PARPs can fully compensate for the loss of PARP1 (Figure 1). Our functional analysis revealed that HeLa *PARP1* KO cells showed reduced proliferation rates and were more sensitive towards the treatment with H_2O_2 and CPT (Figure 2), thereby confirming the central role of PARP1 in genotoxic stress response as previously reported from mouse models, PARP inhibitor, and RNAi studies (73).

Reconstitution studies with the PARP1\E988K mutant verified previous results that this variant acts as a mono- or oligo-(ADP-ribosyl)transferase (Figure 4) (37,53,54). In addition, with regards to its recruitment and release kinetics at sites of laser-induced DNA damage, our results revealed that the PARP1\E988K variant behaves similar in a human cellular system as it does in a mouse system (Figure 5) (55). Thus, as observed by Mortusewicz *et al.*, the PARP1\E988K mutant showed impaired recruitment, yet longer persistence, at sites of DNA damage. Generally, it is thought that localization of PARP1 at sites of DNA damage is regulated by its automodification status, since the presence of the highly negatively charged PAR molecules covalently attached to PARP1 may lead to electrostatic repulsion of PARP1 from negatively charged DNA (74). Our study extended this view by postulating the possibility that non-covalent interaction of PARP1 with PAR via two newly-identified putative PAR binding motifs (PBM1/2) can act as a complementary mechanism in the regulation of the PARP1-DNA interaction (Figure 6). Our finding that PAR inhibits the PARP1-DNA interaction is in agreement with the fact that PBM1 is located in ZnF2, which is necessary for PARP1 binding to DNA strand breaks (5), and that the PBM2 is located at the ZnF3–ZnF1 interface (75). Nevertheless, recruitment studies, showing that a PARP1\PBM mutant exhibits faster release kinetics from sites of DNA damage (data not shown), point to a complex spatio-temporal interplay between PARP1, DNA and PAR. Furthermore, as pointed out by Huambachano *et al.* and Chapman *et al.*, additional PAR binding may occur

via non-classical binding motifs, as identified by these authors (18,62), adding another level of complexity. The analysis and functional relevance of the PARP1–PAR interaction therefore warrants further evaluation.

The impaired recruitment of the PARP1\E988K mutant to DNA damage suggests that initial PAR formation at the site of DNA damage is necessary for subsequent second-wave recruitment of PARP1 molecules (55). In accordance with this, results by Mortusewicz *et al.* show that DNA-binding deficient PARP1 mutants still recruited to sites of laser-induced damage in MEFs and that this recruitment could be inhibited by PARP inhibitor treatment (55). Consistent with our cytotoxicity and cell cycle analyses of CPT-treated, PARP1\E988K-reconstituted HeLa cells (Figures 7 and 8), previous results showed that the PARP1\E988K reconstitution sensitized *Parp1* KO MEFs to CPT treatment in a colony formation assay (51). On the one hand, it is tempting to speculate that these effects can presumably be attributed to trapping of the E988K mutant at sites of DNA damage and therefore manifesting the damage (76). On the other hand, our finding showing that PARP1\E988K expression by itself leads to a G2 arrest, which goes along with higher NAD^+ levels per cell and increased nuclei sizes (Figures 4, 7 and 8), is probably unrelated to a potential trapping effect, since PARP inhibitor treatment completely abolished these effects. In agreement with this, we observed that increased γH2A.X and phospho-RPA2 levels in PARP1\E988K-reconstituted cells can be rescued by PARP inhibitor treatment (Figure 7), suggesting that PARP1\E988K enzymatic activity is able to induce replicative stress. This remarkable possibility suggests that PARP1-mediated mono/oligo-ADP-ribosylation, which may occur upon certain stimuli or as intermediates in PAR catabolism, exerts pronounced and distinct cellular functions.

The PARP1\L713F mutant was originally described as a gain-of-function variant with an over nine times increased K_{cat}, but similar K_m value compared to PARP1\WT (56). These results were recently extended by a biochemical study from Langelier *et al*. These authors demonstrated that the L713F exchange in the hydrophobic core domain (HD) of the catalytic domain (CAT) mimics the effect of DNA damage-induced HD distortions, increasing PARP1 DNA-independent activity up to ∼20-fold and elevating the catalytic efficiency of PARylation while not affecting affinity for NAD^+ (3,57). The HD hydrophobic core mutants studied by Langelier *et al.* did not show an increased level of DNA-dependent activity compared to PARP1\WT, indicating that these mutants act through the same mechanism as DNA to stimulate PARP1 catalytic activity. Our results revealed that the L713F mutant is constitutively active in a cellular environment leading to elevated PAR levels within cells, even without exogenously-induced DNA damage (Figure 4). Thus, PARP1\L713F-reconstituted cells represent a valuable tool to analyze cellular consequences of PAR overproduction with or without application of genotoxic stress. In this regard, our experiments provide first evidence that PAR overproduction or NAD^+ depletion significantly affects cell viability, since PARP1\L713F expression drove cells directly into apoptosis, even without DNA damage induction (Figure 8).

Since PARP1-dependent cell death has implications in several neurodegenerative and neuroinflammatory diseases, such as Parkinson's disease and ischemia reperfusion damage (77), the PARP1\L713F mutant can be very useful to study mechanisms of disease related to PAR overproduction in a cellular setting.

Apart from studying the cellular biochemistry of PARP1 and molecular mechanisms of PARylation, the cell culture model reported in this study can be used to analyze structure–function relationships of naturally occurring *PARP1* variants. One of such variants that has been extensively studied in recent years is a SNP in the *PARP1* gene leading to the V762A aa exchange (35). This variant has been associated with an increased risk for gastric, cervical, and lung cancers and a generally increased cancer risk in the Asian population, while being associated with a decreased risk for brain tumors (38,39). Consistent with the notion that changes in PARP activity might be responsible for these correlations, previous results revealed a reduced enzymatic activity of the PARP1\V762A variant on the biochemical level (36,37). On the other hand, studies of human cells derived of V762A carriers revealed inconsistent results, with one study observing a gene-dose-dependent reduction of PARP activity (78), whereas another one did not find such an effect (79). Our results from reconstituted HeLa *PARP1* KO cells provide clear proof for decreased activity of PARP1\V762A in a cellular environment under conditions of genotoxic stress (Figure 9), thereby strongly supporting a causative link for the increased tumor risk in V762A carriers due to reduced PARP1 activity.

In a patient with pediatric CRC, who inherited a frameshift mutation in *BRCA2* from his father, we identified a maternally inherited missense variant in *PARP1* (F304L) combined with the V762A polymorphism, which significantly reduced PARP1 activity on the biochemical and cellular level. Furthermore, the PARP1\F304L\V762A mutant showed reduced recruitment efficiency to sites of laser-induced DNA damage (Figure 9). The tumor in the CRC patient was deficient for *BRCA2* due to an inherited pathogenic mutation in one allele and an acquired somatic loss of the second wild-type allele. This functional loss of both *BRCA2* alleles, in conjunction with the inherited heterozygous PARP1 variant, may have resulted in an increase in genomic instability and, as a consequence, early-onset of cancer development in the colon. Interestingly, a very recent study by Ding *et al.* demonstrated that pharmacological PARP inhibition or PARP1-silencing in heterozygous *Brca2*$^{-/+}$ mESC resulted in viable homozygous *Brca2*$^{-/-}$ mESC by loss of heterozygosity, a phenomenom termed synthetic viability (80). This genetic constellation very much resembles the one observed in the patient described in the current study. Thus, the drastic impairment of PARP1 activity due to the cumulative effect of the F304L variant and the V762A polymorphism in combination with the *BRCA2* mutation, may well have resulted in predisposition for CCRC development in this patient, however this needs to be clarified in detailed follow-up experiments. Reports on digenic inheritance with germline mutations in genes with synergistic interactions are scarce. This mode of inheritance has been described in patients with extreme phenotypes, i.e. exceptionally early ages of onset or severe clinical presenta-

tions. Examples of these are digenic inheritance in early onset Parkinson's disease [MIM 605909] and severe insulin resistance [MIM 125853] (81,82). On the other hand, in cells deficient in PARylation activity, single-stranded (ss) DNA breaks can accumulate, which, when encountered during DNA replication, may result in the accumulation of double-stranded (ds) DNA breaks. These dsDNA breaks are repaired via HR, which requires proper functioning of BRCA2. Therefore, following the concept of synthetic lethality, cells that are deficient in BRCA2 are highly sensitive to PARP1 inhibition, resulting in cell death by apoptosis (83,84). Thus, complete loss of PARP1 through a second hit in the tumor most likely would have resulted in cell death due to synthetic lethality. Therefore, in retrospect, this patient might have benefited from a PARP1 inhibitor therapy.

In conclusion, this study establishes a novel human cell culture model to decipher the role of PARP1 and PARylation in cellular functions, i.e. a complete *PARP1* KO in HeLa cells. Reconstitution with different PARP1 variants enabled us to study PARP1 hypomorphy (E988K) as well as hypermorphy (F713L) in an easy to handle and exceptionally well-characterized human cancer cell line. Furthermore, we used this approach to correlate epidemiological and clinical findings on naturally occurring PARP1 variants with the cellular properties of these variants. This provides a basis for molecular risk assessment of these and other naturally occurring PARP1 variants in order to judge if carriers may be predisposed to the development of certain diseases.

SUPPLEMENTARY DATA

Supplementary Data are available at NAR Online.

ACKNOWLEDGEMENTS

We like to thank Dr Martin Stöckl for help with 3D deconvolution microscopy, Dr Jennifer Baur for help with the establishment of the KNIME workflow, Felix Schindler for image evaluation, and Dr Roland Nitschke for the LIC macro for automated image acquisition. This study was enabled by the core facilities for light microscopy (Bioimaging Center, Uni KN) and flow cytometry (FlowKON, Uni KN).

FUNDING

Young Scholar Fund (YSF); Research Training Group (RTG) [1331]; Konstanz Research School Chemical Biology (KoRSCB); Collaborative Research Center [CRC969]; DFG grants for scientific instrumentation INST 38/538-1 and INST 38/537-1; *Stichting Kinderen Kankervrij* [KiKa project 127]. Funding for open access charge: University of Konstanz and CRC969.
Conflict of interest statement. None declared.

REFERENCES

1. Hottiger,M.O. (2015) Nuclear ADP-ribosylation and its role in chromatin plasticity, cell differentiation, and epigenetics. *Annu. Rev. Biochem.*, **84**, 227–263.
2. Eustermann,S., Wu,W.F., Langelier,M.F., Yang,J.C., Easton,L.E., Riccio,A.A., Pascal,J.M. and Neuhaus,D. (2015) Structural basis of detection and signaling of DNA single-strand breaks by human PARP-1. *Mol. Cell*, **60**, 742–754.
3. Langelier,M.F., Planck,J.L., Roy,S. and Pascal,J.M. (2012) Structural basis for DNA damage-dependent poly(ADP-ribosyl)ation by human PARP-1. *Science*, **336**, 728–732.
4. Mendoza-Alvarez,H. and Alvarez-Gonzalez,R. (1993) Poly(ADP-ribose) polymerase is a catalytic dimer and the automodification reaction is intermolecular. *J. Biol. Chem.*, **268**, 22575–22580.
5. Ali,A.A., Timinszky,G., Arribas-Bosacoma,R., Kozlowski,M., Hassa,P.O., Hassler,M., Ladurner,A.G., Pearl,L.H. and Oliver,A.W. (2012) The zinc-finger domains of PARP1 cooperate to recognize DNA strand breaks. *Nat. Struct. Mol. Biol.*, **19**, 685–692.
6. Messner,S., Schuermann,D., Altmeyer,M., Kassner,I., Schmidt,D., Schar,P., Muller,S. and Hottiger,M.O. (2009) Sumoylation of poly(ADP-ribose) polymerase 1 inhibits its acetylation and restrains transcriptional coactivator function. *Faseb J.*, **23**, 3978–3989.
7. Walker,J.W., Jijon,H.B. and Madsen,K.L. (2006) AMP-activated protein kinase is a positive regulator of poly(ADP-ribose) polymerase. *Biochem. Biophys. Res. Commun.*, **342**, 336–341.
8. Kauppinen,T.M., Chan,W.Y., Suh,S.W., Wiggins,A.K., Huang,E.J. and Swanson,R.A. (2006) Direct phosphorylation and regulation of poly(ADP-ribose) polymerase-1 by extracellular signal-regulated kinases 1/2. *Proc. Natl. Acad. Sci. U.S.A.*, **103**, 7136–7141.
9. Hassa,P.O., Haenni,S.S., Buerki,C., Meier,N.I., Lane,W.S., Owen,H., Gersbach,M., Imhof,R. and Hottiger,M.O. (2005) Acetylation of poly(ADP-ribose) polymerase-1 by p300/CREB-binding protein regulates coactivation of NF-{kappa}B-dependent transcription. *J. Biol. Chem.*, **280**, 40450–40464.
10. Cohen-Armon,M., Visochek,L., Rozensal,D., Kalal,A., Geistrikh,I., Klein,R., Bendetz-Nezer,S., Yao,Z. and Seger,R. (2007) DNA-independent PARP-1 activation by phosphorylated ERK2 increases Elk1 activity: a link to histone acetylation. *Mol. Cell*, **25**, 297–308.
11. Midorikawa,R., Takei,Y. and Hirokawa,N. (2006) KIF4 motor regulates activity-dependent neuronal survival by suppressing PARP-1 enzymatic activity. *Cell*, **125**, 371–383.
12. Berger,F., Lau,C. and Ziegler,M. (2007) Regulation of poly(ADP-ribose) polymerase 1 activity by the phosphorylation state of the nuclear NAD biosynthetic enzyme NMN adenylyl transferase 1. *Proc. Natl. Acad. Sci. U.S.A.*, **104**, 3765–3770.
13. Guastafierro,T., Cecchinelli,B., Zampieri,M., Reale,A., Riggio,G., Sthandier,O., Zupi,G., Calabrese,L. and Caiafa,P. (2008) CCCTC-binding factor activates PARP-1 affecting DNA methylation machinery. *J. Biol. Chem.*, **283**, 21873–21880.
14. Krukenberg,K.A., Jiang,R., Steen,J.A. and Mitchison,T.J. (2014) Basal activity of a PARP1-NuA4 complex varies dramatically across cancer cell lines. *Cell Rep.*, **8**, 1808–1818.
15. Jungmichel,S., Rosenthal,F., Altmeyer,M., Lukas,J., Hottiger,M.O. and Nielsen,M.L. (2013) Proteome-wide identification of poly(ADP-Ribosyl)ation targets in different genotoxic stress responses. *Mol. Cell*, **52**, 272–285.
16. Zhang,Y., Wang,J., Ding,M. and Yu,Y. (2013) Site-specific characterization of the Asp- and Glu-ADP-ribosylated proteome. *Nat. Methods*, **10**, 981–984.
17. Gagne,J.P., Ethier,C., Defoy,D., Bourassa,S., Langelier,M.F., Riccio,A.A., Pascal,J.M., Moon,K.M., Foster,L.J., Ning,Z. *et al.* (2015) Quantitative site-specific ADP-ribosylation profiling of DNA-dependent PARPs. *DNA Repair*, **30**, 68–79.
18. Chapman,J.D., Gagne,J.P., Poirier,G.G. and Goodlett,D.R. (2013) Mapping PARP-1 auto-ADP-ribosylation sites by liquid chromatography-tandem mass spectrometry. *J. Proteome Res.*, **12**, 1868–1880.
19. Krietsch,J., Rouleau,M., Pic,E., Ethier,C., Dawson,T.M., Dawson,V.L., Masson,J.Y., Poirier,G.G. and Gagne,J.P. (2013) Reprogramming cellular events by poly(ADP-ribose)-binding proteins. *Mol. Aspects Med.*, **34**, 1066–1087.
20. Martello,R., Mangerich,A., Sass,S., Dedon,P.C. and Burkle,A. (2013) Quantification of cellular poly(ADP-ribosyl)ation by stable isotope dilution mass spectrometry reveals tissue- and drug-dependent stress response dynamics. *ACS Chem. Biol*, **8**, 1567–1575.
21. Alvarez-Gonzalez,R., Spring,H., Muller,M. and Bürkle,A. (1999) Selective loss of poly(ADP-ribose) and the 85-kDa fragment of poly(ADP-ribose) polymerase in nucleoli during alkylation-induced apoptosis of HeLa cells. *J. Biol. Chem.*, **274**, 32122–32126.

22. Pascal,J.M. and Ellenberger,T. (2015) The rise and fall of poly(ADP-ribose): an enzymatic perspective. *DNA Repair*, **32**, 10–16.
23. Altmeyer,M., Neelsen,K.J., Teloni,F., Pozdnyakova,I., Pellegrino,S., Grofte,M., Rask,M.B., Streicher,W., Jungmichel,S., Nielsen,M.L. *et al.* (2015) Liquid demixing of intrinsically disordered proteins is seeded by poly(ADP-ribose). *Nat. Commun.*, **6**, 8088.
24. Mangerich,A. and Burkle,A. (2012) Pleiotropic cellular functions of PARP1 in longevity and aging: genome maintenance meets inflammation. *Oxidative Med. Cell. Longevity*, **2012**, 321653.
25. Bai,P. (2015) Biology of poly(ADP-Ribose) polymerases: the factotums of cell maintenance. *Mol. Cell*, **58**, 947–958.
26. Sonnenblick,A., de Azambuja,E., Azim,H.A. Jr and Piccart,M. (2015) An update on PARP inhibitors-moving to the adjuvant setting. *Nat. Rev. Clin. Oncol.*, **12**, 27–41.
27. Curtin,N.J. and Szabo,C. (2013) Therapeutic applications of PARP inhibitors: anticancer therapy and beyond. *Mol. Aspects Med.*, **34**, 1217–1256.
28. Masutani,M., Suzuki,H., Kamada,N., Watanabe,M., Ueda,O., Nozaki,T., Jishage,K., Watanabe,T., Sugimoto,T., Nakagama,H. *et al.* (1999) Poly(ADP-ribose) polymerase gene disruption conferred mice resistant to streptozotocin-induced diabetes. *Proc. Natl. Acad. Sci. U.S.A.*, **96**, 2301–2304.
29. Wang,Z.Q., Auer,B., Stingl,L., Berghammer,H., Haidacher,D., Schweiger,M. and Wagner,E.F. (1995) Mice lacking ADPRT and poly(ADP-ribosyl)ation develop normally but are susceptible to skin disease. *Genes Dev.*, **9**, 509–520.
30. de Murcia,J.M., Niedergang,C., Trucco,C., Ricoul,M., Dutrillaux,B., Mark,M., Oliver,F.J., Masson,M., Dierich,A., LeMeur,M. *et al.* (1997) Requirement of poly(ADP-ribose) polymerase in recovery from DNA damage in mice and in cells. *Proc. Natl. Acad. Sci. U.S.A.*, **94**, 7303–7307.
31. Shall,S. and de Murcia,G. (2000) Poly(ADP-ribose) polymerase-1: what have we learned from the deficient mouse model? *Mutat. Res.*, **460**, 1–15.
32. Blenn,C., Wyrsch,P. and Althaus,F.R. (2012) The sound of silence: RNAi in poly (ADP-Ribose) research. *Genes*, **3**, 779–805.
33. Menissier de Murcia,J., Ricoul,M., Tartier,L., Niedergang,C., Huber,A., Dantzer,F., Schreiber,V., Ame,J.C., Dierich,A., LeMeur,M. *et al.* (2003) Functional interaction between PARP-1 and PARP-2 in chromosome stability and embryonic development in mouse. *EMBO J.*, **22**, 2255–2263.
34. Gibbs-Seymour,I., Fontana,P., Rack,J.G. and Ahel,I. (2016) HPF1/C4orf27 Is a PARP-1-interacting protein that regulates PARP-1 ADP-ribosylation activity. *Mol. Cell*, **62**, 432–442.
35. Cottet,F., Blanche,H., Verasdonck,P., Le Gall,I., Schachter,F., Bürkle,A. and Muiras,M.L. (2000) New polymorphisms in the human poly(ADP-ribose) polymerase-1 coding sequence: lack of association with longevity or with increased cellular poly(ADP-ribosyl)ation capacity. *J. Mol. Med.*, **78**, 431–440.
36. Wang,X.G., Wang,Z.Q., Tong,W.M. and Shen,Y. (2007) PARP1 Val762Ala polymorphism reduces enzymatic activity. *Biochem. Biophys. Res. Commun.*, **354**, 122–126.
37. Beneke,S., Scherr,A.L., Ponath,V., Popp,O. and Bürkle,A. (2010) Enzyme characteristics of recombinant poly(ADP-ribose) polymerases-1 of rat and human origin mirror the correlation between cellular poly(ADP-ribosyl)ation capacity and species-specific life span. *Mech. Ageing Dev.*, **131**, 366–369.
38. Qin,Q., Lu,J., Zhu,H., Xu,L., Cheng,H., Zhan,L., Yang,X., Zhang,C. and Sun,X. (2014) PARP-1 Val762Ala polymorphism and risk of cancer: a meta-analysis based on 39 case-control studies. *PLoS ONE*, **9**, e98022.
39. Hua,R.X., Li,H.P., Liang,Y.B., Zhu,J.H., Zhang,B., Ye,S., Dai,Q.S., Xiong,S.Q., Gu,Y. and Sun,X.Z. (2014) Association between the PARP1 Val762Ala polymorphism and cancer risk: evidence from 43 studies. *PLoS ONE*, **9**, e87057.
40. Beneke,S., Alvarez-Gonzalez,R. and Bürkle,A. (2000) Comparative characterisation of poly(ADP-ribose) polymerase-1 from two mammalian species with different life span. *Exp. Gerontol.*, **35**, 989–1002.
41. Popp,O., Veith,S., Fahrer,J., Bohr,V.A., Burkle,A. and Mangerich,A. (2013) Site-specific noncovalent interaction of the biopolymer poly(ADP-ribose) with the Werner syndrome protein regulates protein functions. *ACS Chem. Biol.*, **8**, 179–188.
42. Pleschke,J.M., Kleczkowska,H.E., Strohm,M. and Althaus,F.R. (2000) Poly(ADP-ribose) binds to specific domains in DNA damage checkpoint proteins. *J. Biol. Chem.*, **275**, 40974–40980.
43. Fahrer,J., Kranaster,R., Altmeyer,M., Marx,A. and Bürkle,A. (2007) Quantitative analysis of the binding affinity of poly(ADP-ribose) to specific binding proteins as a function of chain length. *Nucleic Acids Res.*, **35**, e143.
44. Vissers,L.E., de Ligt,J., Gilissen,C., Janssen,I., Steehouwer,M., de Vries,P., van Lier,B., Arts,P., Wieskamp,N., del Rosario,M. *et al.* (2010) A de novo paradigm for mental retardation. *Nat. Genet.*, **42**, 1109–1112.
45. Hoischen,A., van Bon,B.W., Rodriguez-Santiago,B., Gilissen,C., Vissers,L.E., de Vries,P., Janssen,I., van Lier,B., Hastings,R., Smithson,S.F. *et al.* (2011) De novo nonsense mutations in ASXL1 cause Bohring-Opitz syndrome. *Nat. Genet.*, **43**, 729–731.
46. Landry,J.J., Pyl,P.T., Rausch,T., Zichner,T., Tekkedil,M.M., Stutz,A.M., Jauch,A., Aiyar,R.S., Pau,G., Delhomme,N. *et al.* (2013) The genomic and transcriptomic landscape of a HeLa cell line. *G3*, **3**, 1213–1224.
47. Adey,A., Burton,J.N., Kitzman,J.O., Hiatt,J.B., Lewis,A.P., Martin,B.K., Qiu,R., Lee,C. and Shendure,J. (2013) The haplotype-resolved genome and epigenome of the aneuploid HeLa cancer cell line. *Nature*, **500**, 207–211.
48. Jacobson,E.L. and Jacobson,M.K. (1976) Pyridine nucleotide levels as a function of growth in normal and transformed 3T3 cells. *Arch Biochem. Biophys.*, **175**, 627–634.
49. Beck,C., Robert,I., Reina-San-Martin,B., Schreiber,V. and Dantzer,F. (2014) Poly(ADP-ribose) polymerases in double-strand break repair: Focus on PARP1, PARP2 and PARP3. *Exp. Cell Res.*, **329**, 18–25.
50. Berti,M., Chaudhuri,A.R., Thangavel,S., Gomathinayagam,S., Kenig,S., Vujanovic,M., Odreman,F., Glatter,T., Graziano,S., Mendoza-Maldonado,R. *et al.* (2013) Human RECQ1 promotes restart of replication forks reversed by DNA topoisomerase I inhibition. *Nat. Struct. Mol. Biol.*, **20**, 347–354.
51. Patel,A.G., Flatten,K.S., Schneider,P.A., Dai,N.T., McDonald,J.S., Poirier,G.G. and Kaufmann,S.H. (2012) Enhanced killing of cancer cells by poly(ADP-ribose) polymerase inhibitors and topoisomerase I inhibitors reflects poisoning of both enzymes. *J. Biol. Chem.*, **287**, 4198–4210.
52. Godon,C., Cordelieres,F.P., Biard,D., Giocanti,N., Megnin-Chanet,F., Hall,J. and Favaudon,V. (2008) PARP inhibition versus PARP-1 silencing: different outcomes in terms of single-strand break repair and radiation susceptibility. *Nucleic Acids Res.*, **36**, 4454–4464.
53. Rolli,V., O'Farrell,M., Menissier-de Murcia,J. and de Murcia,G. (1997) Random mutagenesis of the poly(ADP-ribose) polymerase catalytic domain reveals amino acids involved in polymer branching. *Biochemistry*, **36**, 12147–12154.
54. Marsischky,G.T., Wilson,B.A. and Collier,R.J. (1995) Role of glutamic acid 988 of human poly-ADP-ribose polymerase in polymer formation. Evidence for active site similarities to the ADP-ribosylating toxins. *J. Biol. Chem.*, **270**, 3247–3254.
55. Mortusewicz,O., Ame,J.C., Schreiber,V. and Leonhardt,H. (2007) Feedback-regulated poly(ADP-ribosyl)ation by PARP-1 is required for rapid response to DNA damage in living cells. *Nucleic Acids Res.*, **35**, 7665–7675.
56. Miranda,E.A., Dantzer,F., O'Farrell,M., de Murcia,G. and de Murcia,J.M. (1995) Characterisation of a gain-of-function mutant of poly(ADP-ribose) polymerase. *Biochem. Biophys. Res. Commun.*, **212**, 317–325.
57. Dawicki-McKenna,J.M., Langelier,M.F., DeNizio,J.E., Riccio,A.A., Cao,C.D., Karch,K.R., McCauley,M., Steffen,J.D., Black,B.E. and Pascal,J.M. (2015) PARP-1 activation requires local unfolding of an autoinhibitory domain. *Mol. Cell*, **60**, 755–768.
58. Trautlein,D., Deibler,M., Leitenstorfer,A. and Ferrando-May,E. (2010) Specific local induction of DNA strand breaks by infrared multi-photon absorption. *Nucleic Acids Res.*, **38**, e14.
59. Trautlein,D., Adler,F., Moutzouris,K., Jeromin,A., Leitenstorfer,A. and Ferrando-May,E. (2008) Highly versatile confocal microscopy system based on a tunable femtosecond Er:fiber source. *J. Biophoton.*, **1**, 53–61.
60. Haince,J.F., McDonald,D., Rodrigue,A., Dery,U., Masson,J.Y., Hendzel,M.J. and Poirier,G.G. (2008) PARP1-dependent kinetics of

recruitment of MRE11 and NBS1 proteins to multiple DNA damage sites. *J. Biol. Chem.*, **283**, 1197–1208.
61. Robu,M., Shah,R.G., Petitclerc,N., Brind'Amour,J., Kandan-Kulangara,F. and Shah,G.M. (2013) Role of poly(ADP-ribose) polymerase-1 in the removal of UV-induced DNA lesions by nucleotide excision repair. *Proc. Natl. Acad. Sci. U.S.A.*, **110**, 1658–1663.
62. Huambachano,O., Herrera,F., Rancourt,A. and Satoh,M.S. (2010) The double-stranded DNA binding domain of poly(ADP-ribose) polymerase-1 and molecular insight into the regulation of its activity. *J. Biol. Chem.*, **286**, 7149–7160.
63. Umen,J.G. (2005) The elusive sizer. *Curr. Opin. Cell Biol.*, **17**, 435–441.
64. Liu,S., Opiyo,S.O., Manthey,K., Glanzer,J.G., Ashley,A.K., Amerin,C., Troksa,K., Shrivastav,M., Nickoloff,J.A. and Oakley,G.G. (2012) Distinct roles for DNA-PK, ATM and ATR in RPA phosphorylation and checkpoint activation in response to replication stress. *Nucleic Acids Res.*, **40**, 10780–10794.
65. Yu,S.W., Wang,H., Poitras,M.F., Coombs,C., Bowers,W.J., Federoff,H.J., Poirier,G.G., Dawson,T.M. and Dawson,V.L. (2002) Mediation of poly(ADP-ribose) polymerase-1-dependent cell death by apoptosis-inducing factor. *Science*, **297**, 259–263.
66. Wang,Y., Kim,N.S., Haince,J.F., Kang,H.C., David,K.K., Andrabi,S.A., Poirier,G.G., Dawson,V.L. and Dawson,T.M. (2011) Poly(ADP-ribose) (PAR) binding to apoptosis-inducing factor is critical for PAR polymerase-1-dependent cell death (parthanatos). *Sci. Signal.*, **4**, ra20.
67. Fouquerel,E., Goellner,E.M., Yu,Z., Gagne,J.P., Barbi de Moura,M., Feinstein,T., Wheeler,D., Redpath,P., Li,J., Romero,G. *et al.* (2014) ARTD1/PARP1 negatively regulates glycolysis by inhibiting hexokinase 1 independent of NAD+ depletion. *Cell Rep.*, **8**, 1819–1831.
68. Andrabi,S.A., Umanah,G.K., Chang,C., Stevens,D.A., Karuppagounder,S.S., Gagne,J.P., Poirier,G.G., Dawson,V.L. and Dawson,T.M. (2014) Poly(ADP-ribose) polymerase-dependent energy depletion occurs through inhibition of glycolysis. *Proc. Natl. Acad. Sci. U.S.A.*, **111**, 10209–10214.
69. Howlett,N.G., Taniguchi,T., Olson,S., Cox,B., Waisfisz,Q., De Die-Smulders,C., Persky,N., Grompe,M., Joenje,H., Pals,G. *et al.* (2002) Biallelic inactivation of BRCA2 in Fanconi anemia. *Science*, **297**, 606–609.
70. Langelier,M.F., Servent,K.M., Rogers,E.E. and Pascal,J.M. (2008) A Third Zinc-binding Domain of Human Poly(ADP-ribose) Polymerase-1 Coordinates DNA-dependent Enzyme Activation. *J. Biol. Chem.*, **283**, 4105–4114.
71. Desmarais,Y., Menard,L., Lagueux,J. and Poirier,G.G. (1991) Enzymological properties of poly(ADP-ribose)polymerase: characterization of automodification sites and NADase activity. *Biochim. Biophys. Acta*, **1078**, 179–186.
72. Ame,J.C., Rolli,V., Schreiber,V., Niedergang,C., Apiou,F., Decker,P., Muller,S., Hoger,T., Menissier-de Murcia,J. and de Murcia,G. (1999) PARP-2, a novel mammalian DNA damage-dependent poly(ADP-ribose) polymerase. *J. Biol. Chem.*, **274**, 17860–17868.
73. Robert,I., Karicheva,O., Reina San Martin,B., Schreiber,V. and Dantzer,F. (2013) Functional aspects of PARylation in induced and programmed DNA repair processes: preserving genome integrity and modulating physiological events. *Mol. Aspects Med.*, **34**, 1138–1152.
74. Zahradka,P. and Ebisuzaki,K. (1982) A shuttle mechanism for DNA-protein interactions. The regulation of poly(ADP-ribose) polymerase. *Eur. J. Biochem.*, **127**, 579–585.
75. Langelier,M.F. and Pascal,J.M. (2013) PARP-1 mechanism for coupling DNA damage detection to poly(ADP-ribose) synthesis. *Curr. Opin. Struct. Biol.*, **23**, 134–143.
76. Murai,J., Huang,S.Y., Das,B.B., Renaud,A., Zhang,Y., Doroshow,J.H., Ji,J., Takeda,S. and Pommier,Y. (2012) Trapping of PARP1 and PARP2 by Clinical PARP Inhibitors. *Cancer Res.*, **72**, 5588–5599.
77. Fatokun,A.A., Dawson,V.L. and Dawson,T.M. (2014) Parthanatos: mitochondrial-linked mechanisms and therapeutic opportunities. *Br. J. Pharmacol.*, **171**, 2000–2016.
78. Lockett,K.L., Hall,M.C., Xu,J., Zheng,S.L., Berwick,M., Chuang,S.C., Clark,P.E., Cramer,S.D., Lohman,K. and Hu,J.J. (2004) The ADPRT V762A genetic variant contributes to prostate cancer susceptibility and deficient enzyme function. *Cancer Res.*, **64**, 6344–6348.
79. Zaremba,T., Ketzer,P., Cole,M., Coulthard,S., Plummer,E.R. and Curtin,N.J. (2009) Poly(ADP-ribose) polymerase-1 polymorphisms, expression and activity in selected human tumour cell lines. *Br. J. Cancer*, **101**, 256–262.
80. Ding,X., Chaudhuri,A.R., Callen,E., Pang,Y., Biswas,K., Klarmann,K.D., Martin,B.K., Burkett,S., Cleveland,L., Stauffer,S. *et al.* (2016) Synthetic viability by BRCA2 and PARP1/ARTD1 deficiencies. *Nat. Commun.*, **7**, 12425.
81. Savage,D.B., Agostini,M., Barroso,I., Gurnell,M., Luan,J., Meirhaeghe,A., Harding,A.H., Ihrke,G., Rajanayagam,O., Soos,M.A. *et al.* (2002) Digenic inheritance of severe insulin resistance in a human pedigree. *Nat Genet*, **31**, 379–384.
82. Tang,B., Xiong,H., Sun,P., Zhang,Y., Wang,D., Hu,Z., Zhu,Z., Ma,H., Pan,Q., Xia,J.H. *et al.* (2006) Association of PINK1 and DJ-1 confers digenic inheritance of early-onset Parkinson's disease. *Hum Mol Genet*, **15**, 1816–1825.
83. Bryant,H.E., Schultz,N., Thomas,H.D., Parker,K.M., Flower,D., Lopez,E., Kyle,S., Meuth,M., Curtin,N.J. and Helleday,T. (2005) Specific killing of BRCA2-deficient tumours with inhibitors of poly(ADP-ribose) polymerase. *Nature*, **434**, 913–917.
84. Farmer,H., McCabe,N., Lord,C.J., Tutt,A.N., Johnson,D.A., Richardson,T.B., Santarosa,M., Dillon,K.J., Hickson,I., Knights,C. *et al.* (2005) Targeting the DNA repair defect in BRCA mutant cells as a therapeutic strategy. *Nature*, **434**, 917–921.
85. Gagne,J.P., Isabelle,M., Lo,K.S., Bourassa,S., Hendzel,M.J., Dawson,V.L., Dawson,T.M. and Poirier,G.G. (2008) Proteome-wide identification of poly(ADP-ribose) binding proteins and poly(ADP-ribose)-associated protein complexes. *Nucleic Acids Res.*, **36**, 6959–6976.